Journal of Science and Transport Technology
Journal homepage: https://jstt.vn/index.php/en

# Analytical study on nonlinear buckling of spiral-stiffened FG-CNTRC toroidal shells segments with piezoelectric layers and generalized curvature under external pressure

Do Thi Kieu My[1], Kieu Lan Huong[2*], Nguyen Van Tien[3]
[1]Institute for Building Materials and Construction Protection, Institute of Transport Science and Technology, Hanoi, Vietnam
[2]Graduate University of Science and Technology, Vietnam Academy of Science and Technology, Hanoi, Vietnam
[3]Mechanics of Advanced Materials and Structures, University of Transport Technology, Hanoi, Vietnam

**Article info**
**Type of article:**
Original research paper

**DOI:**
https://doi.org/10.58845/jstt.utt.2026.en.6.2.75-97

***Corresponding author:**
Email address:
huongkl@utt.edu.vn

**Received:** 10/09/2025
**Received in Revised Form:** 11/11/2025
**Accepted:** 18/12/2025

**Abstract:** This paper presents an analytical investigation into the nonlinear stability of functionally graded carbon nanotube-reinforced composite (FG-CNTRC) toroidal shell segments with piezoelectric layers and generalized curvature subjected to external pressure. The analysis incorporates several typical meridian shapes, including circular, parabolic, and half-sinusoid geometries. The paper uses Donnell shell theory (DST), combined with von Kármán geometric nonlinearity and an improved Lekhnitskii smeared stiffener technique to study the behavior of stiffened spiral or orthogonal FG-CNTRC shells. The carbon nanotube (CNT) distributions in the shells and stiffeners are designed to satisfy material continuity conditions. Thermal effects and elastic foundation interactions are also incorporated into the analysis, providing a comprehensive framework for understanding their influence on structural stability. To examine large deformation behavior, three-term deflection functions fulfilling the simply supported boundary conditions are adopted, whereas the Ritz energy approach is utilized to derive the load-deflection relationship under external pressure. The numerical results indicate that the critical buckling loads and postbuckling responses are significantly affected by the spiral stiffener system, elastic foundation, temperature variations, and CNT distributions.

**Keywords:** Functionally graded carbon nanotube-reinforced composite, Toroidal shell segment, Ritz energy method, Spiral stiffeners, Generalized meridional curvature.

## 1. Introduction

Toroidal shell segments (T-Ss) and Cylindrical shells (C-Shs) are widely used in various fields, including mechanical, aerospace, and civil engineering, due to their excellent load-bearing capacity. In mechanical and industrial engineering, T-Ss and C-Shs are commonly employed in the fabrication of high-pressure

vessels for liquids and compressed gases. Due to their wide range of applications, from mechanical components to large-scale construction projects, researchers have conducted continuous in-depth investigations into the postbuckling behavior of T-Ss and C-Sh under various types of loads.

In Hutchinson's study [1], Koiter's general theory was employed to investigate the initial postbuckling response of double-curvature shell segments under different loading conditions. The study showed that both the postbuckling behavior and its imperfection sensitivity are highly dependent on the two principal radii of curvature. Ali and Hasan [2] used the Galerkin approach to study the vibration behavior of a functionally graded orthotropic T-Ss, such as concave and convex shell segments, at large amplitudes. Bich et al. [3], Ninh et al. [4], and Thang and Trung [5] investigated the effects of orthogonal stiffener systems arranged on the outer surface of functionally graded material (FGM) T-Ss under various mechanical loadings, including torsion, axial compression, external pressure, and hydrostatic pressure. The results indicated that stiffeners greatly improve the stability and load-bearing capacity, while significantly affecting the nonlinear dynamic buckling response of the FGM T-Ss. The stability and vibration of the FGM C-Sh under linearly increasing dynamic torsional loading were studied and investigated by Sofiyev and Schnack [6], Sofiyev and Kuruoglu [7], and Najafov et al. [8]. Overall, these three studies provided a comprehensive theoretical framework for understanding the torsional vibration and stability behavior of FGM C-Shs under various mechanical and foundation conditions. By using analytical approaches based on the Galerkin method and Pasternak-type elastic foundation models, the authors demonstrated how material distribution laws, orthotropic properties, and foundation stiffness significantly affect the dynamic response and critical torsional load. Comparison between the effects of spiral and orthogonal stiffeners in FGM C-Shs subjected to torsional and external pressure loading was carried out by Phuong et al. [9] and Nam et al. [10,11]. The common point of these studies is the stiffener system arranged inside the C-Sh, and the investigated results confirmed that spiral stiffeners increase the stability and critical loads of the C-Shs more than orthogonal stiffeners.

Graphene-reinforced composites (GRCs) have attracted considerable attention owing to their outstanding mechanical, thermal, and electrical performance. A large number of studies have investigated the static buckling behavior of functionally graded graphene-reinforced composites (FG-GRCs). Moreover, extensive research efforts have been devoted to exploring the mechanical responses of GRC-based structural elements, such as FG-GRC C-Shs and conical shells [12,13], FG-GRC beams and plates [14–18]. The postbuckling behavior and nonlinear dynamic response of sandwich FG-GRC C-Shs under external pressure and low-velocity impact were investigated by Chong Li et al. [19,20]. In these studies, the GRC facesheets were designed to provide the sandwich C-Shs with functionally graded configurations, and 3D double-V meta-lattices were adopted to accommodate the curvature variation of the sandwich shell. Anisotropic FG-GRC stiffeners used to reinforce FG-GRC structures were also investigated by Doan et al. [21,22], Nam et al. [23–25], and Phuong et al. [26,27]. In these studies, the stiffener system was designed so that the volume fraction of graphene at the interface layer between the shell and stiffener was identical, satisfying the functionally graded distribution law.

Carbon nanotubes (CNT) have exceptionally high mechanical strength and stiffness, with outstanding electrical and thermal conductivity. These superior attributes make CNTs ideal reinforcement candidates for advanced composites, with potential applications extending from microelectromechanical systems to aerospace engineering [28]. Following the concept

of FGM, functionally graded carbon nanotube-reinforced composite (FG-CNTRC) structures are designed with CNT volume fractions that are either uniform or linearly change through the thickness. Postbuckling of FG-CNTRC C-Shs under external pressure and axial compression was studied by Shen [29,30]. Following the pioneering work of Shen [31], numerous studies on the buckling and postbuckling behaviors of FG-CNTRC plates and panels were conducted and published by various research groups. Among them, Kiani [32–34] carried out extensive investigations on FG-CNTRC plates subjected to different loading conditions, including thermal and parabolic mechanical loads. Ansari et al. [35] employed a novel numerical variational method to analyze the buckling behavior of FG-CNTRC conical panels under axial loading. By applying the Galerkin procedure, Hieu and Tung [36–38] studied the buckling and postbuckling behaviors of FG-CNTRC T-Ss subjected to uniform external pressure and thermomechanical loadings. Nam et al. [39] used DST to study C-Shs reinforced by CNT arranged in two orthogonal directions.

The aim of this paper is to study the effect of spiral stiffener system on the postbuckling responses of FG-CNTRC T-Ss with piezoelectric layers and generalized curvature under external pressure in thermal environment. The CNT volume fractions are distributed according to the UD, FG-X, FG-O, FG-A, and FG-V patterns across the shell thickness. The temperature-dependent thermo-mechanical properties of the FG-CNTRC are evaluated using the extended rule of mixtures model. The governing equations for FG-CNTRC T-Ss subjected to external pressure are formulated based on Donnell's shell theory combined with the von Kármán-type nonlinear strain-displacement relations, while also accounting for thermal effects. The governing equations are solved by employing the Ritz method, through which the critical loads and postbuckling response curves of the FG-CNTRC T-Ss are obtained.

## 2. T-Ss with piezoelectric layers and generalized meridional curvature

The T-Ss considered in this study have a thickness $h$, a length $L$, and a meridional radius of curvature $a$, as shown in Fig. 1. A piezoelectric layer is attached to the outer surface of shells with a thickness of $h_p$. The shell meridian is examined in three typical configurations as circular, parabolic, and half-sinusoid shapes. The corresponding meridian equations for the parabolic and half-sinusoid T-Ss shells are defined as follows:

$$\begin{aligned} f_{(x)} &= f_{Par} = -\frac{4Hx(L-x)}{L^2}, \\ f_{(x)} &= f_{Sin} = -H\sin\left(\frac{\pi x}{L}\right). \end{aligned} \tag{1}$$

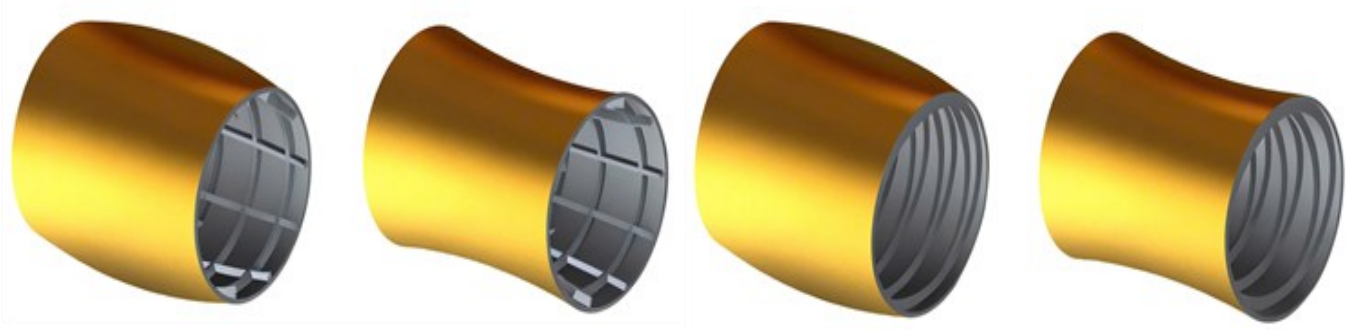

**Fig. 1.** Configurations of orthogonal and spiral stiffened FG-CNTRC T-Ss with generalized meridional curvature

The T-Ss are reinforced by either spiral or orthogonal stiffener systems, with the same geometrical parameters; $b_s, h_s, d_s$ are denoted the width, height, and distance of stiffeners,

respectively. The numbers of stiffeners along the meridional and circumferential directions are represented by $n_S$ and $n_R$. In the case of spiral stiffeners, the number of stiffeners $n_{Sp}$ and the stiffener angle $\theta$ are related together using the expression $\theta = \arccos\left(d_S n_{Sp}/2a\pi\right)$.

The T-S is assumed to rest on a Pasternak-type elastic foundation, and the coordinate system used for the analysis is shown in Fig. 2. Both the shell and stiffeners are fabricated of CNTRC material. In this composite system, CNTs are embedded into the matrix phase either in a uniformly distributed (UD) pattern or in functionally graded (FG) patterns with specific distribution types, namely, FG-V, FG-A, FG-O, and FG-X.

The volume fractions $V_{CNT}$ for five types of CNT distribution are assumed as

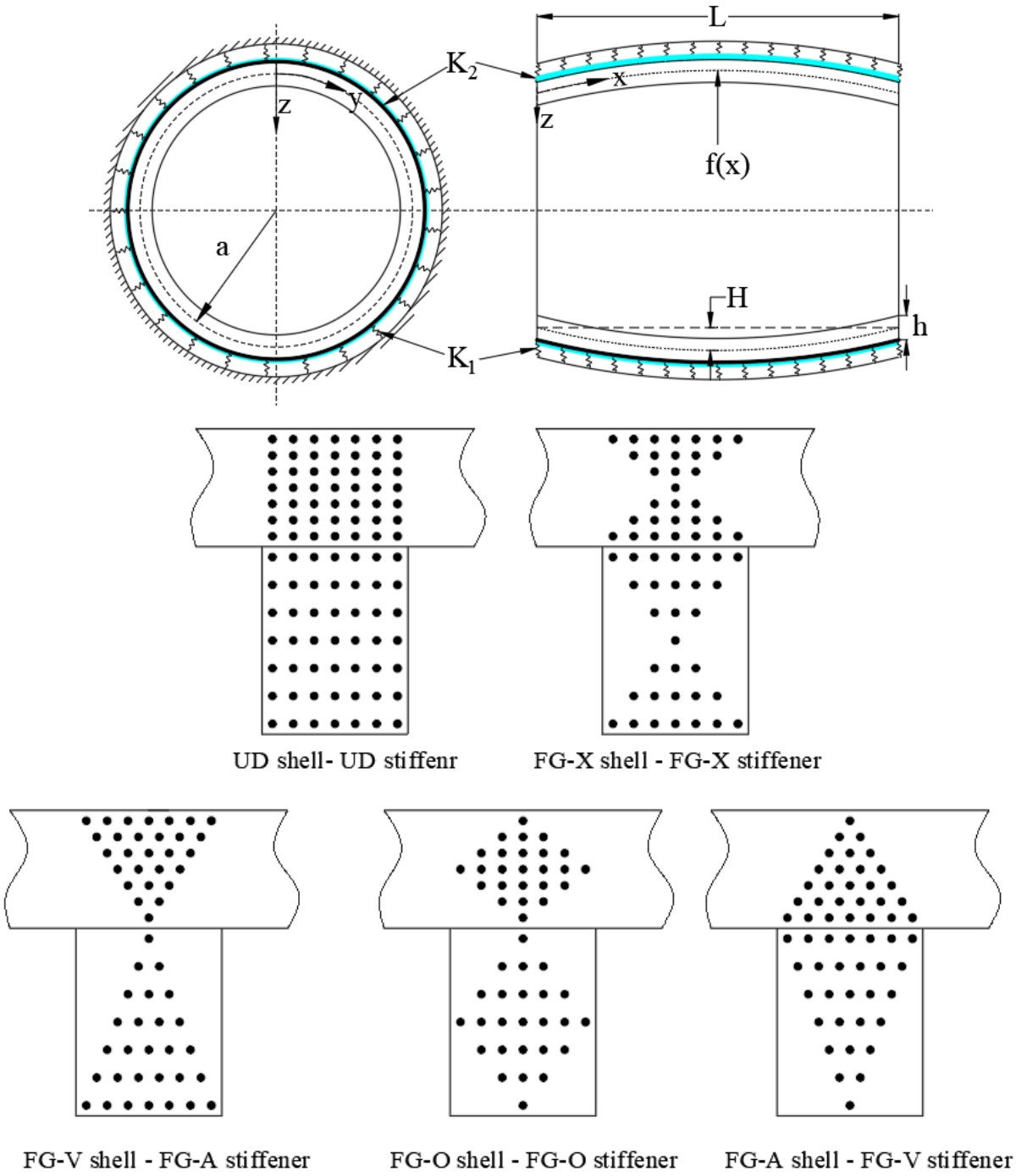


**Fig. 2.** Coordinate system, geometrical properties, and CNT distribution of the T-Ss

$$V_{CNT}=\begin{cases} V_{CNT}^{*}, & -\dfrac{h}{2}\le z\le\dfrac{h}{2} \quad (UD)\\ V_{CNT}^{*}\left(\dfrac{4|z|}{h}\right), & -\dfrac{h}{2}\le z\le\dfrac{h}{2} \quad (FG\text{-}X)\\ V_{CNT}^{*}\left(2-\dfrac{4|z|}{h}\right), & -\dfrac{h}{2}\le z\le\dfrac{h}{2} \quad (FG\text{-}O)\\ V_{CNT}^{*}\left(-\dfrac{2z}{h}+1\right), & -\dfrac{h}{2}\le z\le\dfrac{h}{2} \quad (FG\text{-}V)\\ V_{CNT}^{*}\left(\dfrac{2z}{h}+1\right), & -\dfrac{h}{2}\le z\le\dfrac{h}{2} \quad (FG\text{-}A) \end{cases} \quad (2)$$

To correspond with the CNT distributive law of the shell, the CNT volume fraction of the stiffener is assumed to follow linear functions as follows:

$$V_{CNT}=\begin{cases} V_{CNT}^{*}, & \dfrac{h}{2}\le z\le\dfrac{h}{2}+h_S \ (UD)\\ V_{CNT}^{*}\left|\dfrac{-4z+2h_S+2h}{h_S}\right|, & \dfrac{h}{2}\le z\le\dfrac{h}{2}+h_S \ (FG\text{-}X)\\ V_{CNT}^{*}\left(2-\left|\dfrac{4z-2h_S-2h}{h_S}\right|\right), & \dfrac{h}{2}\le z\le\dfrac{h}{2}+h_S \ (FG\text{-}O)\\ V_{CNT}^{*}\left(\dfrac{-2z+h}{h_S}+2\right), & \dfrac{h}{2}\le z\le\dfrac{h}{2}+h_S \ (FG\text{-}V)\\ V_{CNT}^{*}\left(\dfrac{2z-h}{h_S}\right), & \dfrac{h}{2}\le z\le\dfrac{h}{2}+h_S \ (FG\text{-}A) \end{cases} \quad (3)$$

where

$$V_{CNT}^{*}=\frac{w_{CNT}}{\dfrac{\rho_{CNT}}{\rho_m}-w_{CNT}\dfrac{\rho_{CNT}}{\rho_m}+w_{CNT}}, \quad (4)$$

in which $w_{CNT}$ is the mass fraction of CNTs in the CNTRC shell, and $\rho_{CNT}$ and $\rho_m$ are the densities of the CNTs and matrix, respectively.

According to the extended rule of mixture, the effective Young's moduli and shear modulus can be expressed as [29,30]

$$\frac{\eta_2}{E_{22}}=\frac{V_m}{E^m}+\frac{V_{CNT}}{E_{22}^{CNT}},\quad \frac{\eta_3}{G_{12}}=\frac{V_m}{G^m}+\frac{V_{CNT}}{G_{12}^{CNT}},\quad E_{11}=V_mE^m+\eta_1V_{CNT}E_{11}^{CNT}, \quad (5)$$

where in the above equations, $E_{11}^{CNT}, E_{22}^{CNT}$, and $G_{12}^{CNT}$ are the Young's modulus and shear modulus of single walled CNTs, respectively. Besides, $E^m$ and $G^m$ are Young's modulus and shear modulus, respectively, of the isotropic matrix. The coefficients $\eta_j\,(j=1,2,3)$ are known as the CNT efficiency parameters [29,30].

In addition, $V_{CNT}$ and $V_m$ are the volume fractions of the CNT and the matrix, which satisfy the relationship of $V_{CNT}+V_m=1$.

The coefficients of thermal expansion and Poisson ratio of the CNTRC have the forms [29,30]

$$\begin{aligned} \alpha_{11}&=\alpha_{11}^{CNT}V_{CNT}+\alpha^mV_m,\\ \alpha_{22}&=\left(1+\nu_{12}^{CNT}\right)\alpha_{22}^{CNT}V_{CNT}\\ &\quad+V_m\left(1+\nu^m\right)\alpha^m-\alpha_{11}\nu_{12},\\ \nu_{12}&=V_{CNT}^{*}\nu_{12}^{CNT}+V_m\nu^m, \end{aligned} \quad (6)$$

where $\alpha_{11}^{CNT}, \alpha_{22}^{CNT}$ and $\alpha^m$ are thermal expansion coefficients, and $\nu_{12}^{CNT}$, $\nu^m$ are Poisson's ratios, respectively, of the CNT and matrix

The characteristics of the piezoelectric layer are considered to be temperature-dependent, and determined by

$$\begin{aligned} E_{11P}&=E_{110}+\Delta T.E_{111}.E_{110},\\ G_{12P}&=G_{120}+\Delta T.G_{121}.G_{120},\\ \alpha_{22P}&=\left(1+\Delta T\alpha_{221}\right)\alpha_{220},\\ \alpha_{11P}&=\left(1+\Delta T\alpha_{111}\right)\alpha_{110,} \end{aligned} \quad (7)$$

where $E_{110}, E_{111}, G_{120}, G_{121}, \alpha_{110}, \alpha_{111}, \alpha_{220}, \alpha_{221}$ are the input parameters of the piezoelectric layer, and can be taken by Shen [40].

For the T-Ss, the radius in the curved direction is $R_c$. In the case of parabolic and half-sinusoid T-Ss, the radii in the curved direction can be determined from Eq. (1) respectively, as

$$\begin{aligned} R_{par}&=\frac{1}{8}\frac{\left[L^4+16\left(L^2+4x^2-4Lx\right)H^2\right]^{3/2}}{HL^4},\\ R_{sin}&=\frac{1}{\pi^2LH}\left[\frac{\pi^2H^2}{2}\left(1+\cos\left(\frac{2x\pi}{L}\right)\right)+L^2\right]^{3/2}\times\\ &\quad\left[\sin\left(\frac{\pi x}{L}\right)\right]^{-1}. \end{aligned} \quad (8)$$

## 3. Formulations

According to DST, the components of the strain field on an arbitrary point of the shell may be obtained in terms of those that belong to the mid-surface of the shell [39]

$$\begin{aligned}\varepsilon_{11} &= \varepsilon_{0x} - zw_{,xx},\\ \varepsilon_{22} &= \varepsilon_{0y} - zw_{,yy},\\ \gamma_{12} &= \gamma_{0xy} - 2zw_{,xy},\end{aligned} \tag{9}$$

where

$$\begin{aligned}\varepsilon_{0x} &= u_{,x} + \frac{(w_{,x})^2}{2} - \frac{w}{R},\quad \varepsilon_{0y} = v_{,y} + \frac{(w_{,y})^2}{2} - \frac{w}{a},\\ \gamma_{0xy} &= v_{,x} + u_{,y} + w_{,x}w_{,y},\end{aligned} \tag{10}$$

with $u, v, w$ are the displacement components in $x, y$ and $z$ directions, respectively.

The deformation compatibility equation is obtained from Eq. (10) as follows:

$$\begin{aligned}\varepsilon_{0x,yy} - \gamma_{0xy,xy} + \varepsilon_{0y,xx} &= (w_{,xy})^2 - \frac{w_{,xx}}{a}\\ &\quad - \frac{w_{,yy}}{R_x} - w_{,yy}w_{,xx}.\end{aligned} \tag{11}$$

The stress-strain Hooke law for the unstiffened shells is used in orthotropic form, as

$$\begin{bmatrix}\sigma_{11}\\ \sigma_{22}\\ \sigma_{12}\end{bmatrix} = \begin{bmatrix}Q_{11} & Q_{12} & 0\\ Q_{12} & Q_{22} & 0\\ 0 & 0 & Q_{66}\end{bmatrix}\begin{bmatrix}\varepsilon_{11} - \kappa_1\\ \varepsilon_{22} - \kappa_2\\ \gamma_{12}\end{bmatrix}, \tag{12}$$

where $\kappa_1 = \left(\alpha_{11}\Delta T + \frac{d_{31}}{h_p}V_0\right), \kappa_2 = \left(\alpha_{22}\Delta T + \frac{d_{32}}{h_p}V_0\right)$ and $\Delta T$ is the temperature change with respect to a reference thermal state. $V_0$ is the electric voltage, $d_{31} = d_{32} = 2.54\times10^{-10}\,\mathrm{mV}^{-1}$ and $Q_{ij}$ are the reduced stiffnesses, presented for the piezoelectric layer as

$$\begin{aligned}Q_{11P} &= Q_{22P} = \frac{E_{11P}}{1-\nu_P^2}, Q_{12P} = \frac{\nu_P E_{11P}}{1-\nu_P^2},\\ Q_{66P} &= G_{12P}\end{aligned} \tag{13}$$

and for the FG-CNTRC layer

$$Q_{11SH} = \frac{E_{11}}{1-\nu_{12}\nu_{21}}, Q_{22SH} = \frac{E_{22}}{1-\nu_{12}\nu_{21}},$$

$$Q_{12SH} = \frac{\nu_{21}E_{11}}{1-\nu_{12}\nu_{21}}, Q_{66SH} = G_{12SH}, \tag{14}$$

The forces and moments of stiffened FG-CNTRC T-Ss can be obtained by summing the stiffnesses of shell and stiffeners; the general forms are presented as

$$\begin{Bmatrix}N_x\\ N_y\\ N_{xy}\\ M_x\\ M_y\\ M_{xy}\end{Bmatrix} = \begin{Bmatrix}Z_{11} & Z_{12} & 0 & Y_{11} & Y_{12} & 0\\ Z_{21} & Z_{22} & 0 & Y_{21} & Y_{22} & 0\\ 0 & 0 & Z_{66} & 0 & 0 & Y_{66}\\ Y_{11} & Y_{12} & 0 & D_{11} & D_{12} & 0\\ Y_{21} & Y_{22} & 0 & D_{21} & D_{22} & 0\\ 0 & 0 & Y_{66} & 0 & 0 & D_{66}\end{Bmatrix}\times \begin{Bmatrix}\varepsilon_{0x}\\ \varepsilon_{0y}\\ \gamma_{0xy}\\ -w_{,xx}\\ -w_{,yy}\\ -2w_{,xy}\end{Bmatrix} + \begin{Bmatrix}\Phi_{1x}\\ \Phi_{1y}\\ 0\\ \Phi_{2x}\\ \Phi_{2y}\\ 0\end{Bmatrix}, \tag{15}$$

where $(A_{ij}, B_{ij}, D_{ij})$ represent the stiffness matrix components of shells reinforced by stiffeners and are defined as

$$\begin{aligned}Z_{22} &= Z_{22SH,P} + \mu_2\frac{b_S}{d_S}Z_{11}^{ST} + 2\mu_3\sin^4(\theta)\frac{b_S}{d_S}Z_{11}^{ST},\\ Z_{66} &= Z_{66SH,P} + 2\mu_3\cos^2(\theta)\sin^2(\theta)\frac{b_S}{d_S}Z_{11}^{ST},\\ Z_{11} &= Z_{11SH,P} + \mu_1\frac{b_S}{d_S}Z_{11}^{ST} + 2\mu_3\cos^4(\theta)\frac{b_S}{d_S}Z_{11}^{ST},\\ Z_{12} &= Z_{12SH,P} + 2\mu_3\cos^2(\theta)\sin^2(\theta)\frac{b_S}{d_S}Z_{11}^{ST},\\ Y_{22} &= Y_{22SH,P} + \mu_2\frac{b_S}{d_S}Y_{11}^{ST} + 2\mu_3\frac{b_S}{d_S}Y_{11}^{ST}\sin^4(\theta),\\ Y_{66} &= Y_{66SH,P} + 2\mu_3\frac{b_S}{d_S}Y_{11}^{ST}\cos^2(\theta)\sin^2(\theta),\\ Y_{11} &= Y_{11SH,P} + \mu_1\frac{b_S}{d_S}Y_{11}^{ST} + 2\mu_3\frac{b_S}{d_S}Y_{11}^{ST}\cos^4(\theta),\\ Y_{12} &= Y_{12SH,P} + 2\mu_3\frac{b_S}{d_S}Y_{11}^{ST}\cos^2(\theta)\sin^2(\theta),\\ D_{22} &= D_{22SH,P} + \mu_2\frac{b_S}{d_S}D_{11}^{ST} + 2\mu_3\sin^4(\theta)\frac{b_S}{d_S}D_{11}^{ST},\end{aligned} \tag{16}$$

$$D_{66} = D_{66SH,P} + 2\mu_3 \cos^2(\theta)\sin^2(\theta)\frac{b_S}{d_S}D_{11}^{St},$$

$$D_{11} = D_{11SH,P} + \mu_1\frac{b_S}{d_S}D_{11}^{ST} + 2\mu_3\frac{b_S}{d_S}\cos^4(\theta)D_{11}^{ST},$$

$$D_{12} = D_{12SH,P} + 2\mu_3 \cos^2(\theta)\sin^2(\theta)\frac{b_S}{d_S}D_{11}^{ST},$$

with $\mu_3 = \mu_2 = \mu_1 = 0$ in the case of unstiffened T-Ss, $\mu_3 = 0,\ \mu_1 = \mu_2 = 1$ in the case of orthogonally stiffened T-Ss, and $\mu_3 = 1,\ \mu_1 = \mu_2 = 0$ in the case of spirally stiffened T-Ss, and

$$\left(Z_{ijSH,P},\ Y_{ijSH,P},\ D_{ijSH,P}\right) = \sum\int_{\Pi} Q_{ijSH,P}\left(1,\ z,\ z^2\right)dz, \quad (i,j = 1,2,6),$$

$$\begin{bmatrix} Z_{11}^{ST} & Y_{11}^{ST} \\ Y_{11}^{ST} & D_{11}^{ST} \end{bmatrix} = \sum_{k=1}^{10}\left(\begin{bmatrix} \bar{Z}_{11} & \bar{Y}_{11} \\ \bar{Y}_{11} & \bar{D}_{11} \end{bmatrix} - MT_A.MT_B.\begin{bmatrix} \bar{Z}_{12} & \bar{Y}_{12} \\ 0 & 0 \\ \bar{Y}_{12} & \bar{D}_{12} \\ 0 & 0 \end{bmatrix}\right), \quad (17)$$

where $\Pi$ is the thickness region of the shell, and

$$MT_A = \begin{bmatrix} \bar{Z}_{12} & 0 & \bar{Y}_{12} & 0 \\ \bar{Y}_{12} & 0 & \bar{D}_{12} & 0 \end{bmatrix},$$

$$MT_B = \begin{bmatrix} \bar{Z}_{22} & 0 & \bar{Y}_{22} & 0 \\ 0 & \bar{Z}_{66} & 0 & \bar{Y}_{66} \\ \bar{Y}_{22} & 0 & \bar{D}_{22} & 0 \\ 0 & \bar{Y}_{66} & 0 & \bar{D}_{66} \end{bmatrix}^{-1}, \quad (18)$$

$$\left(\bar{Z}_{ij}, \bar{Y}_{ij}, \bar{D}_{ij}\right)_{(k)} = \frac{b_S}{d_S}\int_{\Delta(k)} Q_{ij(k)}\left(1, z, z^2\right)dz, \quad (i,j = 1,2,6)$$

with $\Delta(k)$ is the thickness region of the stiffeners.

The thermal force expressions of the stiffened shell can be written as

$$\Phi_{1x} = \Phi_{1x}^{SH} + \Phi_{1x}^{P} + \mu_1\frac{b_S}{d_S}\Phi_{1x}^{ST} + 2\mu_3\frac{b_S}{d_S}\Phi_{1x}^{ST} \times \left(\cos^2\theta\sin^4\theta + \cos^4\theta\sin^2\theta + \cos^6\theta\right),$$

$$\Phi_{1y} = \Phi_{1y}^{SH} + \Phi_{1y}^{P} + \mu_2\frac{b_S}{d_S}\Phi_{1x}^{ST} + 2\mu_3\frac{b_S}{d_S}\Phi_{1x}^{ST} \times \left(\sin^2\theta\cos^4\theta + \sin^4\theta\cos^2\theta + \sin^6\theta\right), \quad (19)$$

where

$$\Phi_{1y}^{SH} = \sum_{k=1}^{10}\Delta T\int_{\Pi}\left(Q_{22}\alpha_{22} + Q_{12}\alpha_{11}\right)dz,$$

$$\Phi_{1x}^{SH} = \sum_{k=1}^{10}\Delta T\int_{\Pi}\left(Q_{12}\alpha_{22} + Q_{11}\alpha_{11}\right)dz,$$

$$\Phi_{1x}^{ST} = \sum_{k=1}^{10}\Delta T\int_{\Delta(k)}\left(Q_{12}\alpha_{22} + Q_{11}\alpha_{11}\right)dz, \quad (20)$$

$$\Phi_{1x}^{P} = \int_{\Pi_P}\frac{e_{31}V_0}{h_P}dz,\ \Phi_{1y}^{P} = \int_{\Pi_P}\frac{e_{32}V_0}{h_P}dz$$

where $e_{31}, e_{32}$ are determined as

$$e_{31} = d_{31}Q_{11P} + d_{32}Q_{12P},\ e_{32} = d_{31}Q_{12P} + d_{32}Q_{22P}. \quad (21)$$

From Eq. (15), we have

$$\varepsilon_{0x} = Z_{12}^*\left(N_y - \Phi_{1y}\right) + Z_{11}^*\left(N_x - \Phi_{1x}\right) + Y_{12}^* w_{,yy} + Y_{11}^* w_{,xx},$$

$$\varepsilon_{0y} = Z_{22}^*\left(N_y - \Phi_{1y}\right) + Z_{21}^*\left(N_x - \Phi_{1x}\right) + Y_{22}^* w_{,yy} + Y_{21}^* w_{,xx}, \quad (22)$$

$$\gamma_{0xy} = 2Y_{66}^* w_{,xy} + N_{xy}Z_{66}^*,$$

$$M_x = X_{12}\left(N_y - \Phi_{1y}\right) + X_{11}\left(N_x - \Phi_{1x}\right) + S_{12}w_{,yy} + S_{11}w_{,xx} + \Phi_{2x},$$

$$M_y = X_{22}\left(N_y - \Phi_{1y}\right) + X_{21}\left(N_x - \Phi_{1x}\right) + S_{22}w_{,yy} + S_{21}w_{,xx} + \Phi_{2y}, \quad (23)$$

$$M_{xy} = 2S_{66}w_{,xy} + X_{66}N_{xy},$$

where

$$Z_{12}^* = -\frac{Z_{12}}{\omega_1},\ Z_{11}^* = \frac{Z_{22}}{\omega_1},\ \omega_1 = Z_{11}Z_{22} - Z_{12}Z_{21},$$

$$Y_{12}^* = \frac{Z_{22}Y_{12} - Y_{22}Z_{12}}{\omega_1}, B_{11}^* = \frac{Z_{22}Y_{11} - Z_{12}Y_{21}}{\omega_1},$$

$$Z_{21}^* = -\frac{Z_{21}}{\omega_1},\ Z_{22}^* = \frac{Z_{11}}{\omega_1},\ Y_{22}^* = \frac{Y_{22}Z_{11} - Y_{12}Z_{21}}{\omega_1},$$

$$Y_{21}^* = \frac{Y_{21}Z_{11} - Z_{21}Y_{11}}{\omega_1},\ Y_{66}^* = \frac{Y_{66}}{Z_{66}}, Z_{66}^* = Z_{66}^{-1},$$

$$X_{11} = Y_{11}Z_{11}^* + Y_{12}Z_{21}^*,\ X_{12} = Y_{11}Z_{12}^* + Y_{12}Z_{22}^*,$$

$$X_{22} = Y_{21}Z_{12}^* + Y_{22}Z_{22}^*, X_{21} = Y_{21}Z_{11}^* + Y_{22}Z_{21}^*,$$

$$X_{66} = Y_{66}Z_{66}^*, S_{66} = Y_{66}Y_{66}^* - D_{66},$$

$$S_{12} = Y_{11}Y_{12}^* + Y_{12}Y_{22}^* - D_{12},$$

$$S_{11} = Y_{11}Y_{11}^* + Y_{12}Y_{21}^* - D_{11},$$

$$S_{22} = Y_{21}Y_{12}^* + Y_{22}Y_{22}^* - D_{22},$$

$$S_{21} = Y_{21}Y_{11}^{*} + Y_{22}Y_{21}^{*} - D_{21},$$

The stress function $\psi(x,y)$ satisfied the following conditions can be introduced, as

$$N_x = \psi_{,yy},\ N_{xy} = -\psi_{,xy},\ N_y = \psi_{,xx}. \tag{24}$$

Substituting Eq. (22) and Eq. (24) into Eq. (11), the result is obtained as

$$\begin{aligned}\phi \equiv{}& \psi_{,xxxx}Z_{22}^{*} + \psi_{,yyyy}Z_{11}^{*} + \psi_{,xxyy}\left(Z_{66}^{*} + Z_{12}^{*} + Z_{21}^{*}\right)\\ &+w_{,yyyy}Y_{12}^{*} + w_{,xxxx}Y_{21}^{*} + +w_{,xxyy}\left(Y_{11}^{*} - 2Y_{66}^{*} + Y_{22}^{*}\right)\\ &+\left(w_{,yy} + \frac{1}{a}\right)w_{,xx} + \frac{1}{R_x}w_{,yy} - \left(w_{,xy}\right)^2 = 0.\end{aligned} \tag{25}$$

Tow boundary edges of T-Ss are assumed to be simply supported, and

$$w = M_x = N_x = N_{xy} = 0 \ \text{ at } x = 0, x = L. \tag{26}$$

The deflection in a three-term form of the T-Ss, which satisfies the boundary conditions (26) and stress function, are assumed as follows [41,42]

$$\begin{aligned}w = {}& \gamma_0 + \gamma_1 \sin\left(\frac{ny}{a}\right)\sin\left(\frac{\pi mx}{L}\right)\\ &+ \gamma_2 \sin\left(\frac{\pi mx}{L}\right)^2,\end{aligned} \tag{27}$$

$$\begin{aligned}\psi = {}& \psi_1 \cos\left(\frac{2\pi mx}{L}\right) + \psi_2 \cos\left(\frac{2ny}{a}\right)\\ &+ \psi_3 \sin\left(\frac{\pi mx}{L}\right)\sin\left(\frac{ny}{a}\right)\\ &+ \psi_4 \sin\left(\frac{3\pi mx}{L}\right)\sin\left(\frac{ny}{a}\right) - \frac{\sigma_{oy}hx^2}{2},\end{aligned} \tag{28}$$

where $\gamma_0$, $\gamma_1$ and $\gamma_2$ respectively represent the pre-buckling, linear postbuckling, and nonlinear postbuckling deflection amplitudes. $\sigma_{oy}$ is the circumferential stress. $m$ and $n$ are the buckling modes in the $x$-direction and $y$-direction of the T-Ss, respectively.

In Eq. (8), the curvature in the meridional direction of the parabolic and half-sinusoid T-Ss is not constant. Therefore, the harmonic balance method cannot be applied. By considering the curvature as a function, an approximate technique is employed to determine the coefficients of the stress function, as follows

$$\begin{aligned}&\int_0^{2\pi a}\int_0^{L} \phi.\cos\left(\frac{2\pi mx}{L}\right)dxdy = 0,\\ &\int_0^{2\pi a}\int_0^{L} \phi.\cos\left(\frac{2ny}{a}\right)dxdy = 0,\\ &\int_0^{2\pi a}\int_0^{L} \phi.\sin\left(\frac{\pi mx}{L}\right)\sin\left(\frac{ny}{a}\right)dxdy = 0,\\ &\int_0^{2\pi a}\int_0^{L} \phi.\sin\left(\frac{3\pi mx}{L}\right)\sin\left(\frac{ny}{a}\right)dxdy = 0,\end{aligned} \tag{29}$$

where

$$\begin{aligned}\psi_1 &= a_{1(pa,si,c)}\gamma_1^{\,2} + a_{2(pa,si,c)}\gamma_2,\\ \psi_2 &= a_{3(pa,si,c)}\gamma_1^{\,2},\\ \psi_3 &= a_{4(pa,si,c)}\gamma_1\gamma_2 + a_{5(pa,si,c)}\gamma_1,\\ \psi_4 &= a_{7(pa,si,c)}\gamma_1 + a_{6(pa,si,c)}\gamma_1\gamma_2.\end{aligned} \tag{30}$$

with the subscription $si, pa$, and $c$ are denoted for haft-sinusoid TS-s, parabolic TS-s, and circular T-Ss, and

$$a_{1(pa,si,c)} = \frac{1}{32Z_{22}^{*}}\left(\frac{nL}{ma\pi}\right)^2,$$

$$a_{2(pa,si,c)} = \frac{4m^2Y_{21}^{*}a\pi^2 - L^2}{8m^2Z_{22}^{*}\pi^2 a},$$

$$a_{3(pa,si,c)} = \frac{1}{32Z_{11}^{*}}\left(\frac{ma\pi}{Ln}\right)^2,$$

$$a_{4(pa,si,c)} = -\frac{\left(\pi Lnam\right)^2}{\pi^4m^4a^4Z_{22}^{*} + L^4Z_{11}^{*}n^4 + L^2a^2\delta_1m^2n^2\pi^2},$$

$$\delta_1 = \left(Z_{21}^{*} + Z_{12}^{*} + Z_{66}^{*}\right)$$

$$\begin{aligned}a_{5si} = {}& -\frac{\pi^4a^4Y_{21}^{*}m^4}{\kappa_3} - \frac{L^4Y_{12}^{*}n^4}{\kappa_3}\\ &+ \frac{2a^2\pi^2L^2\left(L^2Hn^2I_{1si} - 0.5\left(-a + n^2\delta_2\right)m^2\right)}{\kappa_3},\end{aligned}$$

$$\kappa_3 = \pi^4a^4Z_{22}^{*}m^4 + L^4Z_{11}^{*}n^4 + L^2a^2m^2\delta_1n^2\pi^2$$

$$\begin{aligned}a_{5pa} = {}& \frac{16a^2n^2HL^7I_{1pa}}{\kappa_3} - \frac{L^4Y_{21}^{*}n^4}{\kappa_3}\\ &+ \frac{-\pi^2a^2m^2\left(-a + \delta_2n^2\right)L^2 - \pi^4Y_{21}^{*}a^4m^4}{\kappa_3},\end{aligned}$$

$$I_{1si}=\int_0^L \sin\left(\frac{x\pi}{L}\right)\left(\sin\left(\frac{m\pi x}{L}\right)\right)^2\times \left(\pi^2H^2\left(\cos\left(\frac{x\pi}{L}\right)\right)^2+L^2\right)^{-3/2}dx,$$

$$I_{1pa}=\int_0^L \frac{1}{\left(16(L-2x)^2H^2+L^4\right)^{3/2}}\left(\sin\left(\frac{m\pi x}{L}\right)\right)^2 dx,$$

$$\delta_2=\left(Y_{11}^*-2Y_{66}^*+Y_{22}^*\right),$$

$$a_{5c}=\frac{\left(-R_cY_{21}^*n^4+n^2a^2\right)L^4}{R_c\kappa_3}-\frac{a^{22}\left(-a+\delta_2n^2\right)m^2\pi L^2}{\kappa_3}-\frac{\pi^4a^4Y_{21}^*m^4}{\kappa_3},$$

$$a_{6(pa,si,c)}=\frac{m^2n^2L^2a^2\pi^2}{\kappa_4},$$

$$a_{7si}=\frac{2n^2L^4H\pi^2I_{2si}a^2}{\kappa_4},$$

$$a_{7pa}=\frac{16L^7n^2Ha^2I_{2pa}}{\kappa_4},$$

$$a_{7c}=0,$$

$$\kappa_4=81\pi^4Z_{22}^*a^4m^4+9L^2a^2n^2\pi^2\delta_1m^2+L^4Z_{11}^*n^4,$$

$$I_{2si}=\int_0^L \frac{\sin\left(\frac{m\pi x}{L}\right)\sin\left(\frac{3m\pi x}{L}\right)\sin\left(\frac{x\pi}{L}\right)}{\left(H^2\left(\cos\left(\frac{x\pi}{L}\right)\right)^2\pi^2+L^2\right)^{3/2}}dx,$$

$$I_{2pa}=\int_0^L \frac{\sin\left(\frac{3m\pi x}{L}\right)\sin\left(\frac{m\pi x}{L}\right)dx}{\left(16(L-2x)^2H^2+L^4\right)^{3/2}}.$$

The closed condition is added in average sense as

$$\int_0^{2\pi a}\int_0^L \frac{\partial v}{\partial y}dxdy=\int_0^{2\pi a}\int_0^L\left(\varepsilon_{0y}+\frac{w}{a}-0.5w_{,y}^2\right)dxdy=0. \quad (31)$$

After performing the necessary calculations, from Eq. (31), the expression for $\sigma_{0y}$ is determined as follows

$$\sigma_{oy}=b_{2(pa,si,c)}\gamma_1^{\,2}+b_{3(pa,si,c)}\gamma_0+b_{4(pa,si,c)}+b_{1(pa,si,c)}\gamma_2, \quad (32)$$

where

$$b_{1(pa,si,c)}=\frac{1}{2Z_{22}^*ha},\ b_{2(pa,si,c)}=-\frac{n^2}{8Z_{22}^*a^2h},$$

$$b_{3(pa,si,c)}=\frac{1}{Z_{22}^*ah},\ b_{4(pa,si,c)}=-\frac{Z_{21}^*\Phi_{1x}+Z_{22}^*\Phi_{1y}}{Z_{22}^*h}.$$

The strain energy of the T-Ss and the work done by the external loads are calculated as

$$U_{in}=\frac{1}{2}\int_{-\frac{h}{2}}^{\frac{h}{2}}\int_0^{2\pi a}\int_0^L\begin{Bmatrix}\sigma_{11}\left(\varepsilon_{11}-\kappa_1\right)\\+\sigma_{22}\left(\varepsilon_{22}-\kappa_2\right)\\+\sigma_{12}\left(\gamma_{12}-\alpha_{12}\Delta T\right)\end{Bmatrix}dxdydz, \quad (33)$$

$$U_{ext}=\int_0^{2\pi a}\int_0^L\left[qw-\frac{1}{2}\left(K_1w-K_2\left(w_{,xx}+w_{,yy}\right)\right)w\right]dxdy. \quad (34)$$

Substituting Eqs. (9), (12), (22), (23), and Eq. (32) into Eq. (33), after simplification, the simple expression has the following form

$$\begin{aligned}U_{in}=&\,g_{1(pa,si,c)}\gamma_0+g_{2(pa,si,c)}\gamma_1^{\,2}+g_{3(pa,si,c)}\gamma_2\\&+c_{0(pa,si,c)}\gamma_1^{\,2}+c_{1(pa,si,c)}\gamma_0^{\,2}+c_{2(pa,si,c)}\gamma_0\gamma_1^{\,2}\\&+c_{3(pa,si,c)}\gamma_0\gamma_2+c_{4(pa,si,c)}\gamma_0+c_{5(pa,si,c)}\gamma_1^{\,4}\\&+c_{6(pa,si,c)}\gamma_2^{\,2}+c_{7(pa,si,c)}\gamma_2+c_{8(pa,si,c)}\\&+c_{9(pa,si,c)}\gamma_1^{\,2}\gamma_2^{\,2}+c_{10(pa,si,c)}\gamma_1^{\,2}\gamma_2+g_{4(pa,si,c)}.\end{aligned} \quad (35)$$

Similarly, substituting Eq. (27) into Eq. (34), the expression can be obtained as

$$\begin{aligned}U_{ext}=&\,t_{1(pa,si,c)}\gamma_1^{\,2}+t_{2(pa,si,c)}\gamma_2^{\,2}-K_1\pi La\gamma_0^{\,2}\\&+2Lq\pi a\gamma_0-\pi K_1La\gamma_0\gamma_2+qL\pi a\gamma_2,\end{aligned} \quad (36)$$

where

$$g_{1(pa,si,c)}=Lhb_{3(pa,si,c)}a\pi\left(Z_{12}^*\Phi_{1x}+Z_{22}^*\Phi_{1y}\right),$$

$$g_{2(pa,si,c)}=Lhb_{2(pa,si,c)}a\pi\left(Z_{12}^*\Phi_{1x}+Z_{22}^*\Phi_{1y}\right),$$

$$g_{3(pa,si,c)}=Lb_{1(pa,si,c)}h\left(Z_{12}^*\Phi_{1x}+Z_{22}^*\Phi_{1y}\right)a\pi,$$

$$\begin{aligned}g_{4(pa,si,c)}=&\frac{L\left(d_{31}\Phi_{1x}+d_{32}\Phi_{1y}\right)\pi aV_0}{h_p}\\&+Lh\left(Z_{12}^*\Phi_{1x}+Z_{22}^*\Phi_{1y}\right)a\pi b_{4(pa,si,c)}\\&+La\pi\left(\Phi_{1x}Z_{11}^*+\Phi_{1y}Z_{12}^*\right)\Phi_{1x}\\&+\Phi_{1y}\left(Z_{21}^*\Phi_{1x}+Z_{22}^*\Phi_{1y}\right)La\pi,\end{aligned}$$

$$c_{0(pa,si,c)} = -\frac{\pi^3\delta_3 m^2 n^2 a_{5(pa,si,c)}}{4aL} + \frac{\pi\kappa_3 a_{5(pa,si,c)}^2}{4L^3a^3} - \frac{\pi^5 S_{11} a m^4}{4L^3} - \frac{\pi S_{22} L n^4}{4a^3} - \frac{\pi^3 S_{66} n^2 m^2}{La} + 2\pi h^2 a L Z_{22}^* b_{2(pa,si,c)} b_{4(pa,si,c)} - \frac{\pi^3 S_{12} m^2 n^2}{4La} + Z_{22}^* \pi h \Phi_{1y} b_{2(pa,si,c)} aL + \pi h a L Z_{21}^* \Phi_{1x} b_{2(pa,si,c)} - \frac{\pi^3 S_{21} m^2 n^2}{4La} + \frac{\pi L a h d_{32} b_{2(pa,si,c)} V_0}{h_p} + \frac{\pi a_7{}^2 \kappa_4}{4L^3a^3} + \frac{\pi\left(m^4\left(Y_{21}^* - X_{12}\right)a^4\pi^4 + n^4L^4\left(Y_{12}^* - X_{21}\right)\right)a_{5(pa,si,c)}}{4L^3a^3},$$

$$\delta_3 = \left(X_{11} - 2X_{66} + X_{22} - \delta_2\right),$$

$$c_{1(pa,si,c)} = Z_{22}^* a\pi h^2 L b_{3(pa,si,c)}^2,$$

$$c_2 = 2Z_{22}^* h^2 a\pi L b_{2(pa,si,c)} b_{3(pa,si,c)},$$

$$c_{3(pa,si,c)} = 2Z_{22}^* a h^2 L\pi b_{3(pa,si,c)} b_{1(pa,si,c)},$$

$$c_{4(pa,si,c)} = \frac{\pi L a h b_{3(si,pa,c)} d_{32} V_0}{h_p} + b_{3(pa,si,c)} h\left(\left(2hb_{4(pa,si,c)} + \Phi_{1y}\right)Z_{22}^* + Z_{21}^*\Phi_{1x}\right)La\pi,$$

$$c_{5(pa,si,c)} = \frac{8\pi^5 Z_{22}^* a_{1(pa,si,c)}^2 a^4 m^4}{a^3L^3} + \frac{\pi L^4 a^4 h^2 Z_{22}^* b_{2(pa,si,c)}^2}{a^3L^3} + \frac{8\pi L^4 n^4 Z_{11}^* a_{3(pa,si,c)}^2}{a^3L^3},$$

$$c_{6(pa,si,c)} = \frac{4\pi m^4 a\left(2Z_{22}^* a_{2(pa,si,c)}^2 - S_{11}/2\right)\pi^4}{L^3} + \frac{4\pi m^4 a}{L^3} a_{2(pa,si,c)}\left(X_{12} - Y_{21}^*\right) + \pi m^4 a Z_{22}^* b_{1(pa,si,c)}^2 h^2 L,$$

$$c_{7(pa,si,c)} = \frac{\pi L a h d_{32} b_{1(pa,si,c)} V_0}{h_p} + ha\pi L Z_{22}^* Z_{21}^* b_{1(pa,si,c)}\Phi_{1x} + b_{1(pa,si,c)} b_{4(pa,si,c)} hha\pi L Z_{22}^* + ha\pi L Z_{22}^*\left(b_{4(pa,si,c)}h + \Phi_{1y}\right)b_{1(pa,si,c)},$$

$$c_{8(pa,si,c)} = b_{4(pa,si,c)}\left(b_{4(pa,si,c)}h + \Phi_{1y}\right)Z_{22}^* hLa\pi + Z_{12}^* hLa\pi b_{4(pa,si,c)}\Phi_{1x},$$

$$c_{9(pa,si,c)} = \frac{m^2n^2\pi^3\left(9a_{6(pa,si,c)}^2 + a_{4(pa,si,c)}^2\right)Z_{12}^*}{4La} + \frac{m^2\pi^3\left(9a_{6(pa,si,c)}^2 + a_{4(pa,si,c)}^2\right)Z_{66}^* n^2}{4La} + \frac{m^4 a Z_{22}^*\left(81a_{6(pa,si,c)}^2 + a_{4(pa,si,c)}^2\right)\pi^5}{4L^3} + \frac{m^2n^2 Z_{21}^*\left(9a_{6(pa,si,c)}^2 + a_{4(pa,si,c)}^2\right)\pi^3}{4La} + \frac{Ln^4\pi\left(a_{6(pa,si,c)}^2 + a_{4(pa,si,c)}^2\right)Z_{11}^*}{4a^3},$$

$$c_{10(pa,si,c)} = \frac{1}{2}\frac{a_{7(pa,si,c)}\kappa_4\pi a_{6(pa,si,c)}}{L^3a^3} + \frac{1}{2}\frac{\pi a_{5(pa,si,c)} a_{4(pa,si,c)}\kappa_3}{L^3a^3} + 2Z_{22}^* Lah^2\pi b_{2(pa,si,c)} b_{1(pa,si,c)} + \frac{1}{4}\frac{\pi a_{4(pa,si,c)}\left(-X_{21} + Y_{12}^*\right)L^4n^4}{L^3a^3} + \frac{1}{4}\frac{a_{4(pa,si,c)}\pi\left(m^4\pi^4\left(Y_{21}^* - X_{12}\right)a^4 - m^2n^2L^2a^2\pi^2\delta_3\right)}{L^3a^3} + \frac{16am^4\pi^5 Z_{22}^* a_{2(pa,si,c)} a_{1(pa,si,c)}}{L^3} + \frac{16m^4\pi^5 a\left(X_{12} - Y_{21}^*\right)a_{1(pa,si,c)}}{4L^3},$$

$$t_{1(pa,si,c)} = -\frac{\left(a^2\left(K_2\pi^2m^2 + L^2K_1\right) + K_2L^2n^2\right)\pi}{4La},$$

$$t_{2(pa,si,c)} = -\frac{3}{8}\frac{\left(\frac{4}{3}\pi^2m^2K_2 + L^2K_1\right)a\pi}{L}.$$

The total potential energy of the system is

$$U_{total} = U_{in} - U_{ext}. \tag{37}$$

Substituting Eqs. (35) and (36) into Eq. (37), the Ritz energy method is then applied as

$$\frac{\partial U_{total}}{\partial\gamma_0} = 0,\ \frac{\partial U_{total}}{\partial\gamma_1} = 0,\ \frac{\partial U_{total}}{\partial\gamma_2} = 0, \tag{38}$$

leads to

$$g_{1(pa,si,c)} + c_{4(pa,si,c)} + \left(2\pi aK_1L + 2c_{1(pa,si,c)}\right)\gamma_0 + K_1\pi aL\gamma_2 - 2Lq\pi a + c_{2(pa,si,c)}\gamma_1{}^2 + c_{3(pa,si,c)}\gamma_2 = 0, \tag{39}$$

$$2c_{5(pa,si,c)}\gamma_1^{\,2} + c_{9(pa,si,c)}\gamma_2^{\,2} + c_{10(pa,si,c)}\gamma_2 + c_{2(pa,si,c)}\gamma_0 - t_{1(pa,si,c)} + g_{2(pa,si,c)} + c_{0(pa,si,c)} = 0, \quad (40)$$

$$K_1 L\pi a\gamma_0 + 2c_{9(pa,si,c)}\gamma_1^{\,2}\gamma_2 - L\pi aq + c_{10(pa,si,c)}\gamma_1^{\,2} - 2t_{2(pa,si,c)}\gamma_2 + c_{3(pa,si,c)}\gamma_0 + g_{3(pa,si,c)} + 2c_{6(pa,si,c)}\gamma_2 + c_{7(pa,si,c)} = 0. \quad (41)$$

From Eq. (39), the expression of $\gamma_0$ can be found as

$$\gamma_0 = \frac{-K_1 L\pi a\gamma_2 + 2L\pi aq - c_{2(pa,si,c)}\gamma_1^{\,2}}{2\left(LK_1\pi a + c_{1(pa,si,c)}\right)} - \frac{c_{4(pa,si,c)} + g_{1(pa,si,c)} + c_{3(pa,si,c)}\gamma_2}{2\left(LK_1\pi a + c_{1(pa,si,c)}\right)}. \quad (42)$$

Substituting Eq. (42) into Eq. (41), the expression of $\gamma_1$ can be obtained as

$$\gamma_1^2 = \frac{q_{5(pa,si,c)} + q.q_{3(pa,si,c)} + q_{4(pa,si,c)}\gamma_2}{q_{2(pa,si,c)} + q_{1(pa,si,c)}\gamma_2}, \quad (43)$$

where

$$q_{1(pa,si,c)} = -4K_1\pi aLc_{9(pa,si,c)} - 4c_{9(pa,si,c)}c_{1(pa,si,c)},$$

$$q_{2(pa,si,c)} = \left(K_1\pi aL + c_{3(pa,si,c)}\right)c_{2(pa,si,c)} - 2\left(K_1\pi aL + c_{1(pa,si,c)}\right)c_{10(pa,si,c)},$$

$$q_{3(pa,si,c)} = -2\pi aL\left(c_{1(pa,si,c)} - c_{3(pa,si,c)}\right),$$

$$q_{4(pa,si,c)} = L\pi a\left(+4c_{6(pa,si,c)} - 2c_{3(pa,si,c)} - 4t_{2(pa,si,c)}\right)K_1 - K_1^{\,2}L^2\pi^2a^2 - c_{3(pa,si,c)}^2 + 4c_{1(pa,si,c)}\left(c_{6(pa,si,c)} - t_{2(pa,si,c)}\right),$$

$$q_{5(pa,si,c)} = 2a\pi LK_1\left(g_{3(pa,si,c)} + c_{7(pa,si,c)}\right) - 2a\pi LK_1\left(g_{1(pa,si,c)} + c_{4(pa,si,c)}\right) + 2\left(c_{7(pa,si,c)} + g_{3(pa,si,c)}\right)c_{1(pa,si,c)} - \left(g_{1(pa,si,c)} + c_{4(pa,si,c)}\right)c_{3(pa,si,c)}.$$

Substituting Eqs. (42) and (43) into Eq. (40), the relationship between q and $\gamma_2$ can be obtained as

$$q = \frac{q_{8(pa,si,c)}\gamma_2^{\,2} + q_{7(pa,si,c)}\gamma_2^{\,3}}{2La\pi q_{1(pa,si,c)}c_{2(pa,si,c)}\gamma_2 + q_{6(pa,si,c)}} + \frac{q_{10(pa,si,c)} + q_{9(pa,si,c)}\gamma_2}{2La\pi q_{1(pa,si,c)}c_{2(pa,si,c)}\gamma_2 + q_{6(pa,si,c)}}, \quad (44)$$

where

$$q_{6(pa,si,c)} = 2La\pi q_{2(pa,si,c)}c_{2(pa,si,c)} + \left(4c_{5(pa,si,c)}\left(\pi aK_1L + c_{1(pa,si,c)}\right) - c_{2(pa,si,c)}^2\right)q_{3(pa,si,c)},$$

$$q_{7(pa,si,c)} = -2q_{1(pa,si,c)}c_{9(pa,si,c)}\left(K_1\pi aL + c_{1(pa,si,c)}\right),$$

$$q_{8(pa,si,c)} = K_1\pi aLq_{1(pa,si,c)}c_{2(pa,si,c)} + c_{3(pa,si,c)}c_{2(pa,si,c)}q_{1(pa,si,c)} - 2q_{1(pa,si,c)}c_{10(pa,si,c)}\left(K_1L\pi a + c_{1(pa,si,c)}\right) - 2q_{2(pa,si,c)}c_{9(s,p,c)}\left(K_1L\pi a + c_{1(pa,si,c)}\right),$$

$$q_{9(pa,si,c)} = -L\pi K_1a\left(2c_{10(pa,si,c)}q_{2(pa,si,c)}\right) - 2La\pi\left(g_{2(pa,si,c)} + c_{0(pa,si,c)} - t_{1(pa,si,c)}\right)K_1q_{1(pa,si,c)} - 4c_{5(pa,si,c)}c_{1(pa,si,c)}q_{4(pa,si,c)} + c_{3(pa,si,c)}c_{2(pa,si,c)}q_{2(pa,si,c)} - L\pi K_1a\left(4c_{5(pa,si,c)}q_{4(pa,si,c)} - q_{2(pa,si,c)}c_{2(pa,si,c)}\right) + 2\left(t_{1(pa,si,c)} - c_{0(pa,si,c)} - g_{2(pa,si,c)}\right)c_{1(pa,si,c)}q_{1(pa,si,c)} + \left(g_{1(pa,si,c)} + c_{4(pa,si,c)}\right)c_{2(pa,si,c)}q_{1(pa,si,c)} - 2c_{10(pa,si,c)}c_{1(pa,si,c)}q_{2(pa,si,c)} + c_{2(pa,si,c)}^2q_{4(pa,si,c)},$$

$$q_{10(pa,si,c)} = -4L\pi aK_1c_{5(pa,si,c)}q_{5(pa,si,c)} - 4c_{5(pa,si,c)}c_{1(pa,si,c)}q_{5(pa,si,c)} + c_{4(pa,si,c)}c_{2(pa,si,c)}q_{2(pa,si,c)} + c_{2(pa,si,c)}^2q_{5(pa,si,c)} + g_{1(pa,si,c)}c_{2(pa,si,c)}q_{2(pa,si,c)} + 2\left(c_{1(pa,si,c)} + K_1L\pi a\right)q_{2(pa,si,c)} \times \left(t_{1(pa,si,c)} - c_{0(pa,si,c)} - g_{2(pa,si,c)}\right)$$

When $\gamma_2 \to 0$ the upper critical buckling pressure for stiffened T-Ss is derived from Eq. (44) as follows

$$q_{up} = \frac{q_{10(pa,si,c)}}{q_{6(pa,si,c)}}. \quad (45)$$

The critical buckling external pressure of

stiffened T-Ss is obtained by using the condition $q_{cr} = \min\left(q_{up}\right)$ versus $(m,n)$.

The maximal deflection expression can be obtained from (27) as

$$W_{max} = \gamma_0 + \gamma_1 + \gamma_2. \quad (46)$$

Substituting Eqs. (42) and (43) into Eq. (46), the expression can be written as

$$W_{max} = \frac{2qL\pi a - L\pi K_1 a\gamma_2 - g_{1(pa,si,c)}}{2\pi K_1 La + 2c_{1(s,p,c)}} - \frac{c_2 q_{6(pa,si,c)} + c_{4(pa,si,c)} + c_{3(pa,si,c)}\gamma_2}{2\pi K_1 La + 2c_{1(s,p,c)}} + \sqrt{q_{6(pa,si,c)}} + \gamma_2 , \quad (47)$$

$$q_{6(pa,si,c)} = \frac{q_{4(pa,si,c)}\gamma_2 + q_{5(pa,si,c)} + q_{3(pa,si,c)}q}{q_{2(pa,si,c)} + q_{1(pa,si,c)}\gamma_2}.$$

Eqs. (44) and (47) can be employed to obtain numerical results and load–deflection curves of stiffened T-Ss subjected to external pressure in thermal environments.

## 4. Results and discussion

### 4.1. Verification

The comparison results shown in Table 1 demonstrate excellent agreement between the present analysis and those reported by Dung and Hoa [43], Shen [44], and Baruch and Singer [45] for isotropic C-Shs under external pressure. For both ring-stiffened and orthogonally-stiffened shells, all studies show the same increasing trend in critical buckling loads.

The critical buckling loads of the C-Sh subjected to external pressure, as presented in Table 2, correlate very well with the findings reported by Shen [29]. Both studies exhibit consistent variations of buckling load with respect to the CNT volume fraction and temperature change. Table 3 further compares the buckling pressure of the FG-CNTRC C-Shs with simply supported boundary conditions. The results show that the critical buckling loads of the cylindrical shells are in good agreement with those reported by Shen [4] and Jam and Kiani [5].

**Table 1.** Comparisons on the critical buckling loads $q_{cr}$ (in Psi) of isotropic C-Shs

| Shell types | Dung and Hoa (DST) [43] | Shen (Boundary layer theory) [44] | Baruch and Singer (DST) [45] | Present (DST) |
|---|---|---|---|---|
| Unstiffened | 103.3271(1,4)[a] | 100.7(1,4) | 102 | 103.327(1,4) |
| Stringer | 104.4937(1,4) | 102.2(1,4) | 103 | 104.494(1,4) |
| Ring | 379.6944(1,3) | 368.3(1,3) | 370 | 379.431(1,3) |
| Orthogonal | 387.1920(1,3) | 374.1(1,3) | 377 | 386.934(1,3) |

[a]The buckling modes $(m,n)$

**Table 2.** Comparisons on the critical buckling loads $q_{cr}$ (in kPa) of CNTRC C-Shs in thermal environment ($a/h = 100$, $h = 1$mm, $L = \sqrt{500ah}$)

| $\Delta T$ | $V^*_{CNT}$ | Shen (HSDT)* [29] | | Present (DST) | |
|---|---|---|---|---|---|
| | | UD | FG-X | UD | FG-X |
| 0 | 0.12 | 18.48(1,7) | 19.91(1,7) | 18.507(1,7) | 19.777(1,7) |
| | 0.17 | 30.81(1,7) | 34.15(1,7) | 30.851(1,7) | 33.936(1,7) |
| | 0.28 | 35.56(1,7) | 43.24(1,7) | 35.621(1,7) | 43.438(1,7) |
| 200 | 0.12 | 14.05(1,7) | 15.17(1,7) | 13.779(1,7) | 14.785(1,7) |
| | 0.17 | 23.32(1,7) | 25.86(1,7) | 22.972(1,7) | 25.343(1,7) |
| | 0.28 | 27.01(1,7) | 28.99(1,7) | 26.553(1,7) | 32.458(1,7) |

* Higher order shear deformation shell theory

**Table 3.** Comparisons on the critical buckling loads $q_{cr}$ (in kPa) of CNTRC C-Shs ($a/h = 30$, $V^*_{CNT} = 0.17$)

| L | | UD | FG-X | FG-V | FG-A |
|---|---|---|---|---|---|
| $\sqrt{300ah}$ | Shen (HSDT) [29] | 433.04(1,4) | 484.05(1,4) | 450.14(1,4) | 404.64(1,4) |
| | Jam and Kiani (DST) [46] | 433.59(1,4) | 478.79(1,4) | 452.81(1,4) | 417.30(1,4) |
| | Present (DST) | 435.34(1,4) | 481.24(1,4) | 454.47(1,4) | 418.50(1,4) |
| $\sqrt{500ah}$ | Shen (HSDT) [29] | 343.81(1,4) | 382.59(1,4) | 357.21(1,4) | 329.24(1,4) |
| | Jam and Kiani (DST) [46] | 344.33(1,4) | 380.02(1,4) | 359.16(1,4) | 339.84(1,4) |
| | Present (DST) | 345.68(1,4) | 381.74(1,4) | 360.42(1,4) | 340.90(1,4) |

Overall, the obtained results provide strong confidence that the proposed method can accurately predict the buckling behavior of FG-CNTRC parabolic T-Ss and half-sinusoid T-Ss under external pressure.

### 4.2. Investigation and discussion

Fig. 3 compares the postbuckling curves of three types of FG-CNTRC T-Ss (half-sinusoid, circular, and parabolic) for both unstiffened and spiral-stiffened configurations. In the unstiffened case (Fig. 3a), all three curves exhibit a similar nonlinear increasing trend in the large deflection domain. The curve of half-sinusoid T-Ss shows a slightly higher postbuckling strength than the other two types, while the curves of circular and parabolic T-Ss almost coincide, indicating that curvature variation has only a minor influence on the postbuckling behavior. In the investigated range, the snap-through phenomenon is clearly observed for the spiral-stiffened shell (see Fig. 3b). Although the overall load–deflection trends of all three shell types are similar, the results summarized in Table 4 reveal a distinct difference in the critical buckling load. Among the three configurations, the half-sinusoid T-Ss exhibits the highest critical buckling loads.

Table 4 clearly demonstrates the substantial effect of both CNT distribution and stiffener types on the critical buckling load of FG-CNTRC T-Ss, and Fig. 4 presents the effect of CNT distributions, stiffener heights, stiffener system and environment temperatures on the postbuckling curves of T-Ss. For the unstiffened shells, the FG-X distribution consistently provides the highest load-bearing capacity across all three shell geometries, while the FG-O pattern proves to be the least effective. However, when orthogonal or spiral stiffeners are added, the critical loads of the FG-V shell are higher than those of the FG-X shell (see Table 4 and Fig. 4a). This result is due to the CNT content being concentrated at the shell and stiffener surfaces, away from the neutral axis, which provides the FG-V shell and FG-A stiffener a higher overall stiffness and enables it to withstand loads more effectively.

The effect of stiffener heights on the postbuckling curves is shown in Fig. 4b. Increasing the stiffener height leads to an increase in the moment of inertia of the cross-section, thereby enhancing the structural stiffness. Figs. 4c,d illustrates the large effects of different stiffener systems on the postbuckling behavior of half-sinusoid and Parabolic T-Ss. Both shell geometries, the addition of any stiffener system significantly increases the critical buckling load, shifting the entire curve upwards. The spiral stiffener consistently provides the highest load-bearing capacity, demonstrating its superior efficiency in resisting external pressure. The effect of environment temperatures change on the postbuckling curves of the half-sinusoid and parabolic T-Ss is displayed in Figs. 4e,f. As the temperature increases, the effective Young's modulus and shear modulus of the composite

decrease sharply. Consequently, the postbuckling curves shift downward, and the critical buckling load exhibits a significant reduction (see Table 5).

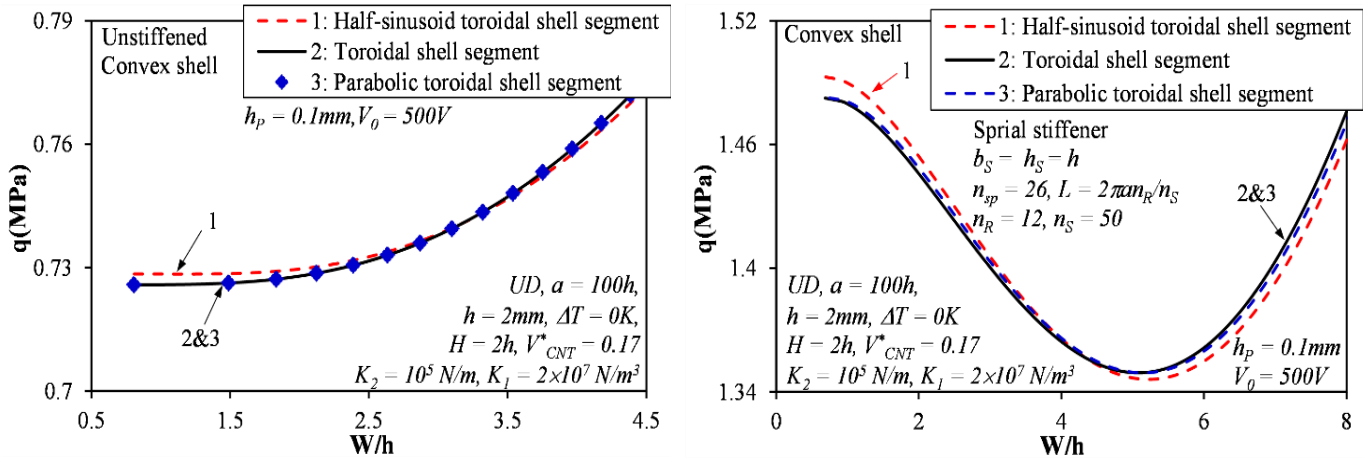


(a) (b)

**Fig. 3.** Comparison of the postbuckling curves of three types of T-Ss in the case of stiffened and unstiffened

**Table 4.** The effect of stiffeners and CNT distribution on the critical buckling loads $q_{cr}$ (MPa) ($\Delta T = 0$, $h = 2$ mm, $h_p = 0.1$mm, $h_S = b_S = h$, $d_S = 2\pi a / n_S$, $a = 100h$, $H = 2h$, $V^*_{CNT} = 0.17$, $L = 2\pi an_R / n_S$, $n_S = 50$, $n_R = 12$, $K_2 = 10^5$ N/m, $K_1 = 2\times10^7$ N/m³)

| Shell | FG-X | UD | FG-O | FG-A | FG-V |
|---|---|---|---|---|---|
| T-Ss | | | | | |
| Unstiffened | 0.732(1,11) | 0.726(1,11) | 0.723(1,11) | 0.732(1,10) | 0.722(1,11) |
| Orthogonal stiffeners | 1.139(1,6) | 1.120(1,6) | 1.104(1,6) | 1.033(1,7) | 1.180(1,6) |
| Spiral stiffeners | 1.507 (1,7,27,57.32)[b] | 1.483 (1,8,26,58.67) | 1.455 (1,8,25,60) | 1.300 (1,8,25,60) | 1.630 (1,7,28,55.94) |
| Parabolic T-Ss | | | | | |
| Unstiffened | 0.732(1,11) | 0.726(1,11) | 0.723(1,11) | 0.732(1,10) | 0.722(1,11) |
| Orthogonal stiffener | 1.139(1,6) | 1.120(1,6) | 1.104(1,6) | 1.033(1,7) | 1.186(1,6) |
| Spiral stiffeners | 1.507 (1,7,27,57.32) | 1.483 (1,8,26,58.67) | 1.455 (1,8,25,60.00) | 1.300 (1,8,25,60.00) | 1.630 (1,7,28,55.94) |
| Half-sinusoid T-Ss | | | | | |
| Unstiffened | 0.734(1,11) | 0.728(1,11) | 0.726(1,11) | 0.735(1,10) | 0.725(1,11) |
| Orthogonal stiffener | 1.144(1,6) | 1.125(1,6) | 1.110(1,6) | 1.037(1,7) | 1.192(1,6) |
| Spiral stiffeners | 1.518 (1,8,27,57.32) | 1.493 (1,8,26,58.67) | 1.465 (1,8,25,60.00) | 1.309 (1,8,25,60.00) | 1.644 (1,7,28,55.94) |

[b] $(m,n,n_{Sp},\theta)$

Fig. 5 presents the effect of CNT volume fraction, a/h ratio, the rise H and the elastic foundation stiffness on the postbuckling curves of T-Ss. Fig. 5a and Table 6 clearly demonstrate that

the volume fraction of CNTs has a significant impact on postbuckling behavior and the critical buckling loads of the T-Ss. As the CNTs volume fraction increases, the composite material becomes stiffer and stronger, thereby increasing the external pressure load-bearing capacity of the T-Ss. Increasing the a/h ratio results in greater shell slenderness, contributing to a reduction in the critical load and lowering the postbuckling curves (see Table 7 and Fig. 5b). In fact, the slenderer the shell is, the more unstable it becomes to instability under loading, which may lead to sudden failure. Conversely, thicker shell will have better load-bearing capacity.

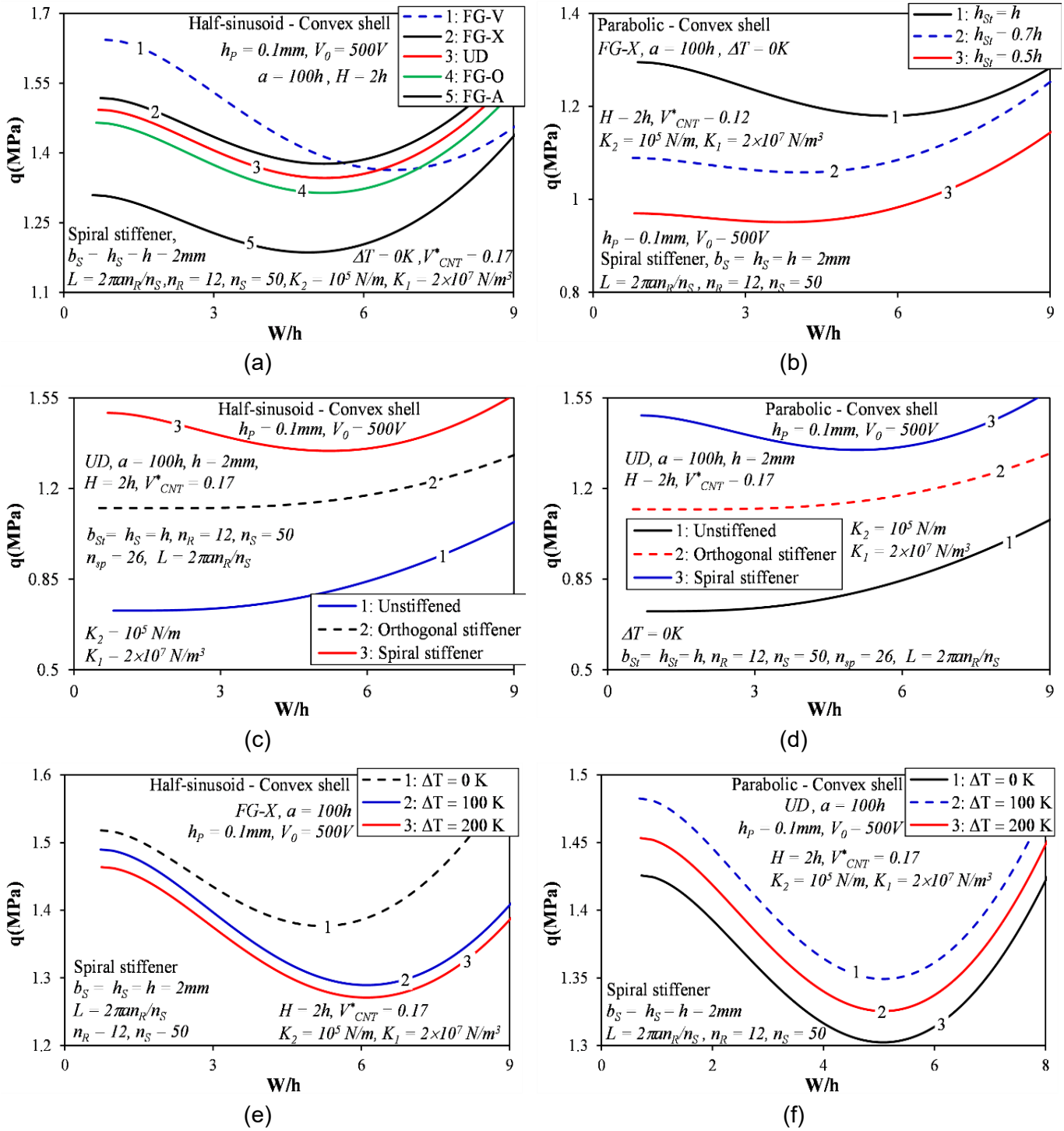


**Fig. 4.** The effect of CNT distributions, stiffener heights, stiffener system and environment temperatures on the postbuckling curves of T-Ss

**Table 5.** The effect of temperature on the critical buckling loads $q_{cri}$ (MPa) of the parabolic and half-sinusoid T-Ss ($h = 2\,mm$, $h_p = 0.1mm$, $h_S = b_S = h$, $d_S = 2\pi a / n_S$, $a = 100h$, Spiral stiffeners, $H = 3h$, $L = 2\pi a n_R / n_S$, $n_S = 50$, $n_R = 12$, $K_2 = 10^5\,N/m$, $K_1 = 2\times10^7\,N/m^3$, $V^*_{CNT} = 0.17$)

| Shell | $\Delta T = 0K$ | $\Delta T = 100K$ | $\Delta T = 200K$ |
|---|---|---|---|
| Half-sinusoid T-Ss | | | |
| UD | 1.617(1,8,26,58.67) | 1.584(1,8,27,57.32) | 1.555(1,8,27,57.32) |
| FG-X | 1.646(1,8,25,60.00) | 1.612(1,8,25,60.00) | 1.581(1,8,26,58.67) |
| FG-V | 1.784(1,8,26,58.67) | 1.744(1,8,26,58.67) | 1.706(1,8,27,57.32) |
| FG-A | 1.431(1,8,27,57.32) | 1.405(1,8,27,57.32) | 1.381(1,8,27,57.32) |
| FG-O | 1.593(1,8,27,57.32) | 1.562(1,8,28,55.94) | 1.533(1,8,28,55.94) |
| Parabolic T-Ss | | | |
| UD | 1.598(1,8,26,58.67) | 1.566(1,8,26,58.67) | 1.536(1,8,27,57.32) |
| FG-X | 1.628(1,8,24,61.31) | 1.595(1,8,25,60.00) | 1.563(1,8,26,58.67) |
| FG-V | 1.765(1,8,26,58.67) | 1.725(1,8,26,58.67) | 1.686(1,8,26,58.67) |
| FG-A | 1.412(1,8,27,57.32) | 1.387(1,8,28,55.94) | 1.364(1,9,28,55.94) |
| FG-O | 1.573(1,8,27,57.32) | 1.542(1,8,28,55.94) | 1.513(1,8,28,55.94) |

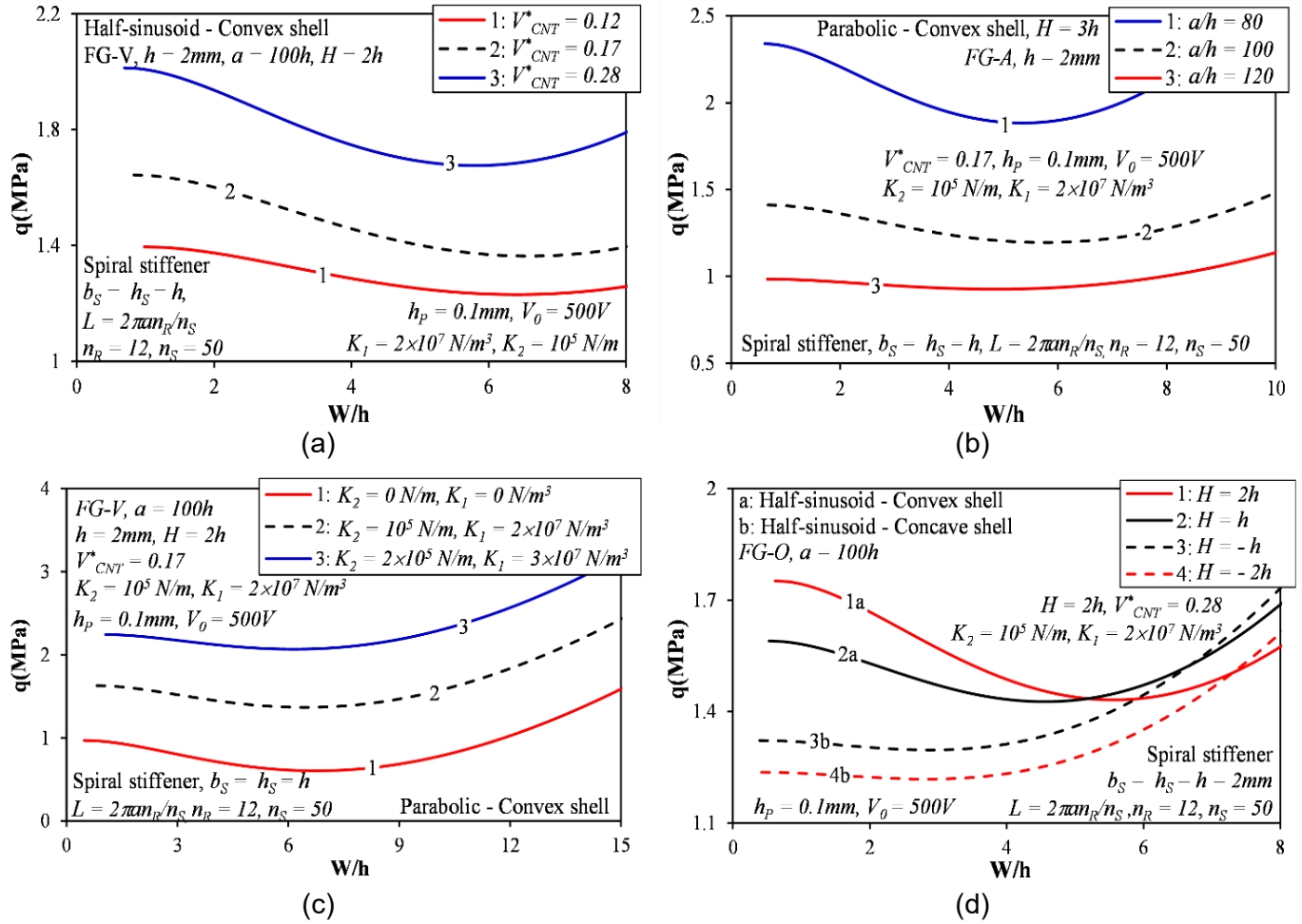


**Fig. 5.** The effect of CNT volume fraction, a/h ratio, the rise H and the elastic foundation stiffness on the postbuckling curves of T-Ss

**Table 6.** The effect of $V_{CNT}^{*}$ on the critical buckling loads $q_{cri}$ (MPa) of the parabolic and half-sinusoid T-Ss ($h = 2\,mm,\ h_p = 0.1mm,\ h_S = b_S = h,\ d_S = 2\pi a / n_S,\ a = 100h,$ Spiral stiffeners, $H = 3h,\ L = 2\pi a n_R / n_S,\ n_S = 50,\ n_R = 12,\ K_2 = 10^5\ N/m,\ K_1 = 2\times10^7\ N/m^3,\ \Delta T = 0K$)

| Shell | $V_{CNT}^{*} = 0.12$ | $V_{CNT}^{*} = 0.17$ | $V_{CNT}^{*} = 0.28$ |
|---|---|---|---|
| Half-sinusoid T-Ss | | | |
| UD | 1.377(1,8,25,60.00) | 1.617(1,8,26,58.67) | 1.985(1,8,29,54.55) |
| FG-X | 1.398(1,8,24,61.31) | 1.646(1,8,25,60.00) | 2.028(1,8,27,57.32) |
| FG-V | 1.499(1,8,26,58.67) | 1.784(1,8,26,58.67) | 2.219(1,8,29,54.55) |
| Parabolic T-Ss | | | |
| UD | 1.364 (1,8,25,60.00) | 1.598(1,8,26,58.67) | 1.954(1,8,29,54.55) |
| FG-X | 1.384 (1,8,25,60.00) | 1.628(1,8,24,61.31) | 1.994(1,8,29,54.55) |
| FG-V | 1.485 (1,8,26,58.67) | 1.765(1,8,26,58.67) | 2.187(1,8,28,55.94) |

**Table 7.** The effect of $a/h$ ratio on the critical buckling loads $q_{cri}$ (MPa) of parabolic and haft-sinusoid T-Ss ($\Delta T = 0K,\ h = 2\,mm,\ h_p = 0.1mm,\ h_S = b_S = h,\ d_S = 2\pi a / n_S,$ Spiral stiffeners, $H = 2h,\ L = 2\pi a n_R / n_S,\ n_S = 50,\ n_R = 12,\ K_2 = 10^5\ N/m,\ K_1 = 2\times10^7\ N/m^3,\ V_{CNT}^{*} = 0.12$)

| Shell | $a/h = 80$ | $a/h = 100$ | $a/h = 120$ |
|---|---|---|---|
| Half-sinusoid T-Ss | | | |
| UD | 2.047(1,7,27,57.32) | 1.289(1,8,26,58.67) | 0.924(1,8,24,61.31) |
| FG-X | 2.084(1,7,26,58.67) | 1.304(1,7,27,57.32) | 0.935(1,8,23,62.61) |
| FG-V | 2.260(1,7,27,57.32) | 1.395(1,7,28,55.94) | 0.990(1,8,24,61.31) |
| FG-A | 1.803(1,7,28,55.94) | 1.155(1,8,24,61.31) | 0.850(1,8,25,60.00) |
| FG-O | 2.014(1,7,28,55.94) | 1.270(1,8,25,60.00) | 0.913(1,8,26,58.67) |
| Parabolic T-Ss | | | |
| UD | 2.029(1,7,27,57.32) | 1.280(1,7,26,58.67) | 0.920(1,8,24,61.31) |
| FG-X | 2.066(1,7,26,58.67) | 1.291(1,8,28,55.94) | 0.931(1,8,23,62.61) |
| FG-V | 2.241(1,7,27,57.32) | 1.385(1,7,28,55.94) | 0.986(1,8,24,61.31) |
| FG-A | 1.786(1,7,28,55.94) | 1.148(1,8,24,61.31) | 0.846(1,8,25,60.00) |
| FG-O | 1.995(1,7,28,55.94) | 1.262 (1,7,25,60.00) | 0.909(1,8,25,60.00) |

The elastic foundation generates a reaction force that resists the shell's deflection. As the foundation stiffness increases, this reaction force becomes stronger, thereby stiffening the overall structure and reducing the shell's susceptibility to deformation under loading. Varying the elastic foundation stiffness also changes the critical load and postbuckling curves of the TS-s (see Table 8 and Fig. 5c). The effects of the rise H on the postbuckling curves and critical buckling load are displayed in Fig. 5d and Table 9. As the H increases, the load-bearing capacity of the shell also increases, and the postbuckling curves vary accordingly. For the concave shell, the parabolic TS-s exhibits a slightly higher load-bearing capacity than the half-sinusoid T-Ss.

**Table 8.** The effect of foundation stiffnesses on the critical buckling loads $q_{cri}$ (MPa) ($\Delta T = 0K$, $h = 2\,mm$, $h_p = 0.1mm$, $h_S = b_S = h$, $d_S = 2\pi a / n_S$, $a = 100h$, Spiral stiffeners, $H = 2h$, $L = 2\pi a n_R / n_S$, $n_S = 50$, $n_R = 12$, $V^*_{CNT} = 0.28$)

| $K_1$ (N/m$^3$), $K_2$ (N/m) | FG-V | UD | FG-X |
|---|---|---|---|
| Half-sinusoid T-Ss | | | |
| 0, 0 | 1.379(1,7,29,54.55) | 1.166(1,8,27,57.32) | 1.209(1,7,28,55.94) |
| $2\times10^7$, $10^5$ | 2.013(1,8,27,57.32) | 1.787(1,8,27,57.32) | 1.841(1,8,26,58.67) |
| $5\times10^7$, $5\times10^5$ | 4.376(1,8,30,53.13) | 4.142(1,8,28,55.94) | 4.191(1,8,28,55.94) |
| Parabolic T-Ss | | | |
| 0, 0 | 1.358(1,7,29,54.55) | 1.147(1,7,27,57.32) | 1.179(1,7,26,58.67) |
| $2\times10^7$, $10^5$ | 1.996(1,8,27,57.32) | 1.769(1,8,27,57.32) | 1.825(1,8,26,58.67) |
| $5\times10^7$, $5\times10^5$ | 4.358(1,8,29,54.55) | 4.126(1,8,28,55.94) | 4.174(1,8,28,55.94) |

**Table 9.** The effect of the rise $H$ on the critical buckling loads $q_{cr}$ (MPa) of three types of perfect shells ($\Delta T = 0K$ $h = 2\,mm$, $h_p = 0.1mm$, $a = 100h$, $h_S = b_S = h$, $d_S = 2\pi a / n_S$, $K_2 = 10^5$ N/m, $K_1 = 2\times10^7$ N/m$^3$, Spiral stiffeners, $L = 2\pi a n_R / n_S$, $n_S = 50$, $n_R = 12$, $V^*_{CNT} = 0.28$, $\Delta T = 0K$)

| | $H = h$ | $H = 2h$ | $H = 3h$ | $H = -h$ | $H = -2h$ | $H = -3h$ |
|---|---|---|---|---|---|---|
| | | | Half-sinusoid T-Ss | | | |
| UD | 1.625 (1,8,28,55.94) | 1.787 (1,8,27,57.32) | 1.985 (1,8,29,54.55) | 1.363 (1,7,24,61.31) | 1.265 (1,6,27,57.32) | 1.204 (1,6,20,66.42) |
| FG-X | 1.664 (1,7,28,55.94) | 1.841 (1,8,26,58.67) | 2.028 (1,8,27,57.32) | 1.411 (1,6,25,60.00) | 1.305 (1,6,25,60.00) | 1.256 (1,6,18,68.90) |
| FG-V | 1.820 (1,7,29,54.55) | 2.013 (1,8,27,57.32) | 2.219 (1,8,29,54.55) | 1.526 (1,7,27,57.32) | 1.404 (1,6,28,55.94) | 1.323 (1,6,24,61.31) |
| FG-A | 1.389 (1,8,25,60.00) | 1.537 (1,8,28,55.94) | 1.711 (1,9,26,58.67) | 1.171 (1,7,23,62.61) | 1.110 (1,6,26,58.67) | 1.061 (1,6,18,68.90) |
| FG-O | 1.590 (1,8,27,57.32) | 1.752 (1,8,28,55.94) | 1.956 (1,8,28,55.94) | 1.322 (1,7,25,60.00) | 1.237 (1,6,28,55.94) | 1.167 (1,6,23,62.61) |
| | | | Parabolic T-Ss | | | |
| UD | 1.617 (1,7,28,55.94) | 1.771 (1,8,27,57.32) | 1.954 (1,8,29,54.55) | 1.367 (1,7,24,61.31) | 1.273 (1,6,27,57.32) | 1.208 (1,6,21,65.17) |
| FG-X | 1.656 (1,7,28,55.94) | 1.825 (1,8,26,58.67) | 1.999 (1,8,27,57.32) | 1.416 (1,6,25,60.00) | 1.312 (1,6,25,60.00) | 1.258 (1,6,17,70.12) |
| FG-V | 1.811 (1,7,29,54.55) | 1.996 (1,8,27,57.32) | 2.187 (1,8,28,55.94) | 1.533 (1,6,26,58.67) | 1.414 (1,6,29,54.55) | 1.330 (1,6,25,60.00) |
| FG-A | 1.384 (1,8,25,60.00) | 1.522 (1,8,28,55.94) | 1.687 (1,9,27,57.32) | 1.174 (1,7,23,62.61) | 1.115 (1,6,25,60.00) | 1.063 (1,6,20,66.42) |
| FG-O | 1.584 (1,8,27,57.32) | 1.735 (1,8,28,55.94) | 1.928 (1,8,29,54.55) | 1.326 (1,7,25,60.00) | 1.245 (1,6,28,55.94) | 1.172 (1,6,24,61.31) |

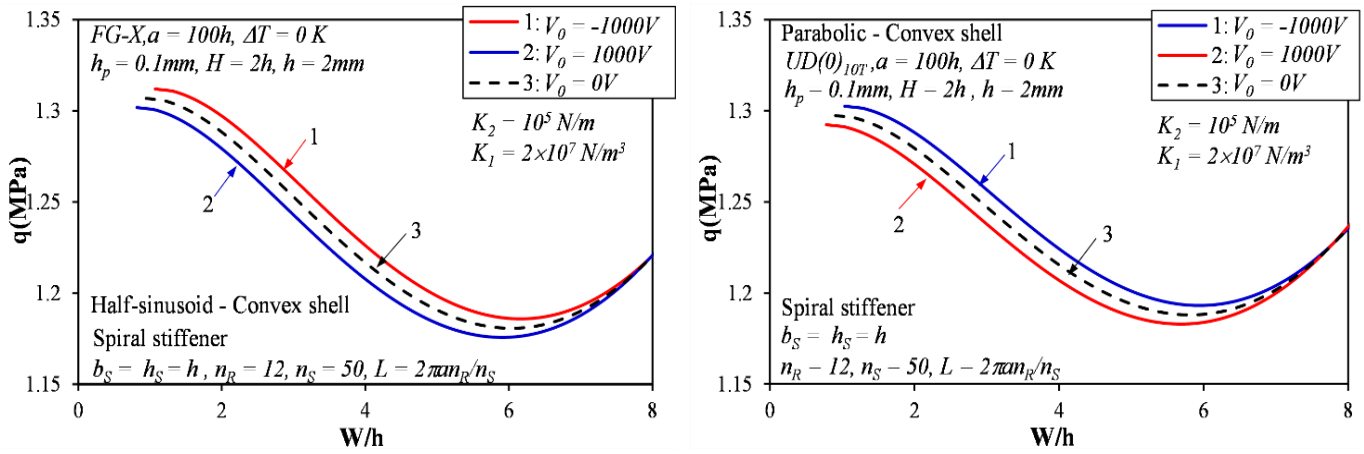


**Fig. 6.** The effect of the electric voltage $V_0$ on the postbuckling curves of T-Ss

Fig. 6 illustrates the postbuckling behavior of half-sinusoid and Parabolic T-Ss under the effect of an applied electric voltage $V_0$. Variations in the applied voltage cause changes in the mechanical and electrical characteristics of the piezoelectric layer. These altered properties then affect the load–strain interaction, which directly changes the postbuckling behavior.

## 5. Conclusions

Based on a simple and effective analytical approach, the buckling behavior of spiral-stiffened FG-CNTRC T-Ss with piezoelectric layers and generalized curvature under external pressure has been analyzed. Formulations are based on the DST and von Kármán geometric nonlinearity, combined with the improved Lekhnitskii smeared stiffener approach. The Ritz energy approach is applied to find the load–deflection relationship under external pressure. The changes in elastic foundation stiffness, temperature, slenderness, the rise H, and CNT distribution patterns were considered and investigated in the paper. The results obtained should be noted as follows

1. The stiffener system greatly improves the buckling resistance, with the spiral stiffeners offering the most significant enhancement compared to the orthogonal and unstiffened configurations.

2. On the postbuckling curves, the snap-through phenomenon is observed when the shell is reinforced with spiral stiffeners.

3. The postbuckling trends of the three types of shell are similar. Among them, the postbuckling curves of the circular and parabolic T-Ss shells almost completely coincide.

Overall, this paper provides an efficient and accurate approach for predicting the nonlinear stability and postbuckling behavior of spiral-stiffened FG-CNTRC T-Ss with piezoelectric layers and generalized curvature. The findings can serve as a useful reference for the optimal design and stability control of advanced FG-CNTRC shell structures integrated with piezoelectric layers.

## References

[1] J.W. Hutchinson. (1967). Initial post-buckling behavior of toroidal shell segments. *International Journal of Solids and Structures*, 3(1), 97–115. https://doi.org/10.1016/0020-7683(67)90046-7

[2] A.Y. Ali, H.M. Hasan. (2022). Non-linear large amplitude vibration of orthotropic FGM convex and concave toroidal shell segments including the damping effect using the shear deformation theory. *Thin-Walled Structures*, 173, 109035. https://doi.org/10.1016/j.tws.2022.109035

[3] B.H. Dao, N.G. Dinh, T.I. Tran. (2016). Buckling Analysis of Eccentrically Stiffened Functionally Graded Toroidal Shell Segments under Mechanical Load. *Journal of Engineering*

*Mechanics*, 142(1), 04015054. https://doi.org/10.1061/(ASCE)EM.1943-7889.0000964

[4] D.G. Ninh, D.H. Bich, B.H. Kien. (2015). Torsional buckling and post-buckling behavior of eccentrically stiffened functionally graded toroidal shell segments surrounded by an elastic medium. *Acta Mechanica*, 226(10), 3501–3519. https://doi.org/10.1007/s00707-015-1391-6

[5] P.-T. Thang, T. Nguyen-Thoi. (2016). A new approach for nonlinear dynamic buckling of S-FGM toroidal shell segments with axial and circumferential stiffeners. *Aerospace Science and Technology*, 53, 1–9. https://doi.org/10.1016/j.ast.2016.03.008

[6] A.H. Sofiyev, E. Schnack. (2004). The stability of functionally graded cylindrical shells under linearly increasing dynamic torsional loading. *Engineering Structures*, 26(10), 1321–1331. https://doi.org/10.1016/j.engstruct.2004.03.016

[7] A.H. Sofiyev, N. Kuruoglu. (2013). Torsional vibration and buckling of the cylindrical shell with functionally graded coatings surrounded by an elastic medium. *Composites Part B: Engineering*, 45(1), 1133–1142. https://doi.org/10.1016/j.compositesb.2012.09.046

[8] A.M. Najafov, A.H. Sofiyev, N. Kuruoglu. (2013). Torsional vibration and stability of functionally graded orthotropic cylindrical shells on elastic foundations. *Meccanica*, 48(4), 829–840. https://doi.org/10.1007/s11012-012-9636-0

[9] N. Thi Phuong, D. Thanh Luan, V.H. Nam, P.T. Hieu. (2019). Nonlinear approach on torsional buckling and postbuckling of functionally graded cylindrical shells reinforced by orthogonal and spiral stiffeners in thermal environment. *Proceedings of the Institution of Mechanical Engineers, Part C: Journal of Mechanical Engineering Science*, 233(6), 2091–2106. https://doi.org/10.1177/0954406218780523

[10] V.H. Nam, N.T. Phuong, N.T. Trung. (2019). Nonlinear buckling and postbuckling of sandwich FGM cylindrical shells reinforced by spiral stiffeners under torsion loads in thermal environment. *Acta Mechanica*, 230(9), 3183–3204. https://doi.org/10.1007/s00707-019-02452-5

[11] V.H. Nam, N.T. Phuong, C.V. Doan, N.T. Trung. (2019). Nonlinear Thermo-Mechanical Stability Analysis of Eccentrically Spiral Stiffened Sandwich Functionally Graded Cylindrical Shells Subjected to External Pressure. *International Journal of Applied Mechanics*, 11(05), 1950045. https://doi.org/10.1142/S1758825119500455

[12] H.-S. Shen, Y. Xiang. (2018). Postbuckling of functionally graded graphene-reinforced composite laminated cylindrical shells subjected to external pressure in thermal environments. *Thin-Walled Structures*, 124, 151–160. https://doi.org/10.1016/j.tws.2017.12.005

[13] Y. Kiani. (2019). Buckling of functionally graded graphene reinforced conical shells under external pressure in thermal environment. *Composites Part B: Engineering*, 156, 128–137. https://doi.org/10.1016/j.compositesb.2018.08.052

[14] Y. Kiani, M. Mirzaei. (2018). Enhancement of non-linear thermal stability of temperature dependent laminated beams with graphene reinforcements. *Composite Structures*, 186, 114–122. https://doi.org/10.1016/j.compstruct.2017.11.086

[15] H. Mohammadi, Y. Kiani. (2024). Isogeometric nonlinear free vibration analysis of FG-GRC laminated Timoshenko beams with temperature-dependent material properties. *Structures*, 67, 106910. https://doi.org/10.1016/j.istruc.2024.106910

[16] M. Mirzaei, Y. Kiani. (2017). Isogeometric thermal buckling analysis of temperature dependent FG graphene reinforced laminated plates using NURBS formulation. *Composite Structures*, 180, 606–616. https://doi.org/10.1016/j.compstruct.2017.08.057

[17] M. Karimi Zeverdejani, Y. Tadi Beni, Y. Kiani. (2020). Multi-Scale Buckling and Post-Buckling Analysis of Functionally Graded Laminated Composite Plates Reinforced by Defective Graphene Sheets. *International Journal of Structural Stability and Dynamics*, 20(01), 2050001. https://doi.org/10.1142/S0219455420500017

[18] F. Abbaspour, H. Arvin, Y. Kiani. (2022). Mechanical buckling analysis of functionally graded composite laminated plates reinforced with temperature dependent graphene sheets resting on elastic foundation. *ZAMM - Journal of Applied Mathematics and Mechanics / Zeitschrift für Angewandte Mathematik und Mechanik*, 102(1), e202100097. https://doi.org/10.1002/zamm.202100097

[19] C. Li, J. Yang, H.-S. Shen. (2022). Postbuckling of pressure-loaded auxetic sandwich cylindrical shells with FG-GRC facesheets and 3D double-V meta-lattice core. *Thin-Walled Structures*, 177, 109440. https://doi.org/10.1016/j.tws.2022.109440

[20] C. Li, H.-S. Shen, J. Yang. (2022). Low-velocity impact response of cylindrical sandwich shells with auxetic 3D double-V meta-lattice core and FG GRC facesheets. *Ocean Engineering*, 262, 112299. https://doi.org/10.1016/j.oceaneng.2022.112299

[21] C.V. Doan, V.T. Hung, N.T. Phuong, V.H. Nam. (2023). Torsional buckling and postbuckling behavior of stiffened FG-GRCL toroidal shell segments surrounded by elastic foundation. *International Journal of Computational Materials Science and Engineering*, 12(03), 2350001. https://doi.org/10.1142/S204768412350001X

[22] V.D. Cao, H.N. Vu, T.P. Nguyen. (2023). Nonlinear Electro-Thermo-Torsional Buckling Analysis of Stiffened Functionally Graded Graphene-Reinforced Composite Laminated Toroidal Shell Segments. *Journal of Engineering Mechanics*, 149(2), 04022106. https://doi.org/10.1061/JENMDT.EMENG-6607

[23] H.N. Vu, T.P. Nguyen, S.L. Ho, M.D. Vu, V.D. Cao. (2023). Nonlinear buckling analysis of stiffened FG-GRC laminated cylindrical shells subjected to axial compressive load in thermal environment. *Mechanics Based Design of Structures and Machines*, 51(7), 3678–3694. https://doi.org/10.1080/15397734.2021.1932522

[24] V.H. Nam, D.T. Dong, C.V. Doan, N.T. Phuong. (2022). Nonlinear Thermo-Electro-Mechanical Buckling of Higher-Order Shear Deformable Stiffened FG-GRC Laminated Plates. *International Journal of Applied Mechanics*, 14(06), 2250051. https://doi.org/10.1142/S175882512250051X

[25] V.H. Nam, D.T. Dong, C. Van Doan, N.T. Phuong. (2022). Nonlinear buckling of axially compressed FG-GRCL stiffened cylindrical panels with a piezoelectric layer by using Reddy's higher-order shear deformation theory. *Polymer Composites*, 43(11), 7952–7966. https://doi.org/10.1002/pc.26931

[26] N.T. Phuong, D.T. Dong, C. Van Doan, V.H. Nam. (2022). Nonlinear buckling of higher-order shear deformable stiffened FG-GRC laminated plates with nonlinear elastic foundation subjected to combined loads. *Aerospace Science and Technology*, 127, 107736. https://doi.org/10.1016/j.ast.2022.107736

[27] N.T. Phuong, D.T. Dong, C. Van Doan, V.H. Nam. (2023). Nonlinear buckling of stiffened FG-GRCL cylindrical panels under axial compression with the uniformly distributed temperature variation. *The European Physical Journal Plus*, 138(3), 234. https://doi.org/10.1140/epjp/s13360-023-03841-5

[28] O. Gohardani, M.C. Elola, C. Elizetxea. (2014). Potential and prospective implementation of carbon nanotubes on next generation aircraft and space vehicles: A review of current and expected applications in aerospace sciences. *Progress in Aerospace Sciences*, 70, 42–68.

https://doi.org/10.1016/j.paerosci.2014.05.002

[29] H.-S. Shen. (2011). Postbuckling of nanotube-reinforced composite cylindrical shells in thermal environments, Part II: Pressure-loaded shells. *Composite Structures*, 93(10), 2496–2503. https://doi.org/10.1016/j.compstruct.2011.04.005

[30] H.-S. Shen. (2011). Postbuckling of nanotube-reinforced composite cylindrical shells in thermal environments, Part I: Axially-loaded shells. *Composite Structures*, 93(8), 2096–2108. https://doi.org/10.1016/j.compstruct.2011.02.011

[31] H.-S. Shen. (2009). Nonlinear bending of functionally graded carbon nanotube-reinforced composite plates in thermal environments. *Composite Structures*, 91(1), 9–19. https://doi.org/10.1016/j.compstruct.2009.04.026

[32] Y. Kiani. (2017). Thermal buckling of temperature-dependent FG-CNT-reinforced composite skew plates. *Journal of Thermal Stresses*, 40(11), 1442–1460. https://doi.org/10.1080/01495739.2017.1336742

[33] Y. Kiani. (2017). Buckling of FG-CNT-reinforced composite plates subjected to parabolic loading. *Acta Mechanica*, 228(4), 1303–1319. https://doi.org/10.1007/s00707-016-1781-4

[34] Y. Kiani. (2018). Thermal post-buckling of temperature dependent sandwich plates with FG-CNTRC face sheets. *Journal of Thermal Stresses*, 41(7), 866–882. https://doi.org/10.1080/01495739.2018.1425645

[35] R. Ansari, J. Torabi, M.F. Shojaei, E. Hasrati. (2016). Buckling analysis of axially-loaded functionally graded carbon nanotube-reinforced composite conical panels using a novel numerical variational method. *Composite Structures*, 157, 398–411. https://doi.org/10.1016/j.compstruct.2016.08.028

[36] H.V. Tung, P.T. Hieu. (2018). Nonlinear buckling of CNT-reinforced composite toroidal shell segment surrounded by an elastic medium and subjected to uniform external pressure. *Vietnam Journal of Mechanics*, 40(3), 285–301. https://doi.org/10.15625/0866-7136/12397

[37] P.T. Hieu, H.V. Tung. (2020). Postbuckling Behavior of Carbon-Nanotube-Reinforced Composite Toroidal Shell Segments Subjected to Thermomechanical Loadings. *AIAA Journal*, 58(7), 3187–3198. https://doi.org/10.2514/1.J059055

[38] P.T. Hieu, H. Van Tung. (2019). Thermomechanical nonlinear buckling of pressure-loaded carbon nanotube reinforced composite toroidal shell segment surrounded by an elastic medium with tangentially restrained edges. *Proceedings of the Institution of Mechanical Engineers, Part C: Journal of Mechanical Engineering Science*, 233(9), 3193–3207. https://doi.org/10.1177/0954406218802942

[39] V.H. Nam, N.-T. Trung, N.T. Phuong, V.M. Duc, V.T. Hung. (2020). Nonlinear Torsional Buckling of Functionally Graded Carbon Nanotube Orthogonally Reinforced Composite Cylindrical Shells in Thermal Environment. *International Journal of Applied Mechanics*, 12(07), 2050072. https://doi.org/10.1142/S1758825120500726

[40] H.-S. Shen. (2005). Postbuckling of FGM plates with piezoelectric actuators under thermo-electro-mechanical loadings. *International Journal of Solids and Structures*, 42(23), 6101–6121. https://doi.org/10.1016/j.ijsolstr.2005.03.042

[41] A.S. Volmir. (1972). Non-linear dynamics of plates and shells. Nauka, Russian. (In Russian)

[42] A.S. Volmir. (1956). Flexible plates and shells. State Publishing House of Technical and Theoretical Literature, Moscow. (In Russian)

[43] D.V. Dung, L.K. Hoa. (2013). Nonlinear buckling and post-buckling analysis of eccentrically stiffened functionally graded circular cylindrical shells under external pressure. Thin-Walled Structures, 63, 117–124.

https://doi.org/10.1016/j.tws.2012.09.010

[44] H.-S. Shen. (1997). Post-buckling analysis of imperfect stiffened laminated cylindrical shells under combined external pressure and axial compression. Computers & Structures, 63(2), 335–348. https://doi.org/10.1016/S0045-7949(96)00341-0

[45] M. Baruch, J. Singer. (1963). Effect of Eccentricity of Stiffeners on the General Instability of Stiffened Cylindrical Shells under Hydrostatic Pressure. Journal of Mechanical Engineering Science, 5(1), 23–27. https://doi.org/10.1243/JMES_JOUR_1963_005_005_02

[46] J.E. Jam, Y. Kiani. (2015). Buckling of pressurized functionally graded carbon nanotube reinforced conical shells. Composite Structures, 125, 586–595. https://doi.org/10.1016/j.compstruct.2015.02.052